Wound-responsive dressing for delivery of bioactive molecules

Filipe Costa
Master in Applications in Biotechnology and Synthetic Biology
Departments of Biology and Chemistry and Biochemistry
Faculty of Sciences of the University of Porto
2024/2025

Wound-responsive dressing for delivery of bioactive molecules

Filipe Costa

Dissertation carried out as part of the Master in Applications in Biotechnology and Synthetic Biology

Departments of Biology and Chemistry and Biochemistry

2024/2025

Supervisor
Cristina Martins, Principal Investigator, “i3S- Instituto de Investigação e Inovação em Saúde- Universidade do Porto”

Co-supervisor
Pedro Moreno, Associate Researcher, “i3S- Instituto de Investigação e Inovação em Saúde- Universidade do Porto”



Acknowledgements

Dada por finalizada esta etapa, gostava de agradecer, primeiramente à minha equipa de orientação. Queria agradecer à Claúdia Monteiro, pela ideia do projeto que desenvolvemos e pelos ensinamentos teóricos que me transmitiu ao longo dos últimos meses. De seguida, gostava de agradecer, com um grande abraço, ao Pedro Moreno, por me ter ensinado imenso, especialmente no início, por todas as horas que passou comigo a discutir resultados e em sessões intensivas de brainstorming. Por me ter motivado sempre nos momentos em que tudo parecia desabar. O meu muito obrigado! Por fim, queria agradecer à Professora Cristina Martins, minha orientadora principal, que sempre me acolheu muito bem, sempre muito disponível, inclusive fins de semana e feriados. Obrigado por me apoiar desde o início, por me ter aceite no grupo e por todos os bons conselhos que me deu, não só no contexto de trabalho, mas a nível pessoal também. O meu profundo obrigado!

Para além disso, gostava de agradecer aos meus colegas de grupo, à Beatriz, à Rita, à Catarina, ao Diogo, à Clara, à Paula, à Joana Barros, à Joana Marques (que provavelmente ainda não viu o filme que recomendei), à Luísa (que deve ter ido ao WC), à Sofia (que faz bolos deliciosos), à Rute (que foi embora no dia em que escrevo estes agradecimentos), ao Tiago (obrigado velhinho, por todas as aulas de química, és um rapaz muito divertido, gosto de ti) e, por fim, a pessoa que tem o lugar mais especial nesta lista, sem qualquer dúvida, pois sem ela eu não saberia o que fazer da minha vida… agradeço imenso a todos por serem tão bons colegas, por proporcionarem um ambiente de trabalho tão saudável e por me terem ajudado sempre que precisei… mas de facto tenho de agradecer sobretudo à Filipa Campos, por ser, para mim, um grande exemplo como profissional. Obrigado por me teres “adotado”, por me acompanhares sempre, mesmo quando te custa, por me ensinares tanto. Graças a ti, cresci imenso, sou melhor, por te ver como um exemplo. És uma excelente profissional, gosto muito de ti!

Para além disso gostava de agradecer a outras pessoas que me ajudaram durante o decorrer deste projeto. Ao Pedro Alves, um grande obrigado. Foi graças a ti que descobri este grupo e foste tu que me suscitaste o interesse nesta área. Obrigado, também pelos ensinamentos iniciais e pela disponibilidade (pós-laboral) e por me teres introduzido a toda esta gente maravilhosa. Queria agradecer ao Ricardo Vidal, à Maria Lazaro e à Dalila por serem pessoas excelentes e me terem ajudado sempre que possível na

execução de algumas técnicas. Ao senhor Carlos, por me ter arranjado os LEDs uma série de vezes.

Agora, falando das pessoas que melhor me conhecem, queria agradecer aos meus Amigos do peito, que sempre me apoiam, alguns deles desde criança (hahaha ainda sou…), David, Pedro, Nuno, Teresa, Raul, Riczão (tropinha do i3s), Zezoca, Carlos, Daniela. Os meus amigos do curso, Daniel, David A., Aimone, Beatriz, Pedro, Filipa e a Inês Mota, obrigado por tornarem os meus anos académicos mais divertidos. Que os vossos copos estejam sempre cheios, para brindarmos muitas vezes! À minha família, que são pessoas incríveis e sempre me apoiaram em todos os desafios da vida.

Claro que não podia esquecer-me de uma pessoa tão especial, a minha namorada, Catarina. Obrigado, Amor, por seres tão compreensiva comigo, sempre, por me apoiares, por me incentivares a ser melhor, por me dares na cabeça quando é necessário…. Obrigado por fazeres parte da minha vida e espero que nela continues, para podermos partilhar as nossas conquistas, sempre (minha cientista <3!!)

Também gostava de agradecer a uma pessoa que sempre foi muito especial para mim. Infelizmente, já há algum tempo que cá não está, mas é alguém por quem tenho imenso respeito e que guardo para sempre no meu ser. Queria deixar um grande beijinho à Avó Isaura, de quem eu tenho muitas saudades e que de certeza está orgulhosa do meu percurso até aqui.

Eu sei que isto ainda não é uma tese de doutoramento, mas eu sou uma pessoa muito emotiva… enfim. Imaginem como seria num doutoramento …

Por último, e NUNCA menos importante, queria agradecer aos meus pais, por toda a educação que me deram, pelo quanto investiram em mim para eu ser quem sou, o quanto sacrificaram para me darem tudo, sou um privilegiado por nada me faltar! É graças a eles que pude viajar a minha vida toda, que tive uma infância incrível, da qual tenho imensas saudades, que nasci, (óbvio!), num ambiente familiar incrível, cheia de pessoas especiais, e claro, que me pude licenciar e, se tudo correr bem, me tornar mestre. Eu sei que é difícil perceberem o que eu faço da vida (ou o que quero fazer), inclusive, às vezes, nem eu sei, mas espero que estejam orgulhosos e que se continuem a orgulhar das minhas conquistas, que partilharei sempre convosco.

Obrigado, Pai, pelos sacrifícios que fizeste na tua vida! Obrigado pelos ensinamentos, pela sabedoria, pela paciência, pelos caracóis (hahahah), pelas brincadeiras, por alinhares comigo nos parques aquáticos, no snorkeling, no pádel... obrigado por seres o melhor Pai do Mundo! Espero um dia ser, pelo menos, metade do Homem que tu és…

Obrigado, Mãe, por seres a melhor amiga, melhor conselheira, a dona da razão (porque Mãe tem sempre razão), pelas noites mal dormidas, por me ires buscar sabe-se lá onde durante a noite, por veres o meu melhor e o meu pior, por estares sempre lá! Por me teres passado o bom gosto, o olhar desconfiado, o stress, a educação… E por todo o mimo Mãezinha!

Amo-vos muito!

Para terminar, gostava de deixar uma nota para mim próprio. Talvez para ler um dia mais tarde, quando duvidar das minhas capacidades. Esta foi a minha primeira experiência de trabalho e acho que me fez muito bem. Não imaginava que fazer um mestrado fosse tão stressante e desafiador, ao ponto de me levar aos meus limites. Acho que nunca me senti tão empenhado em algo, como neste período que estive a desenvolver este trabalho. Tantas vezes duvidei, tantas vezes chorei de desespero, suei imenso (porque de facto isto faz suar), até sangrei (do nariz) … literalmente sangue, suor e lágrimas… Crazy!

Como é óbvio que nesta fase ainda não sei qual a nota que me vão dar, mas sinto que foi a experiência mais enriquecedora que alguma vez tive e foi aqui que senti que, afinal, quero fazer ciência. Pelo menos nos próximos anos. Com jeitinho, isto ainda me leva a dar uma volta ao mundo a falar sobre coisas que acho que descobri, quando andava a pipetar coisinhas para tubos e placas…

Mas fica a minha nota de superação, de sentimento de missão cumprida e de orgulho em mim próprio… Parabéns puto, conseguiste!

Resumo

Feridas crónicas representam um grande desafio clínico devido à inflamação persistente e a infeções bacterianas recorrentes, particularmente por *Pseudomonas aeruginosa* e *Staphylococcus aureus*. Este estudo tem como objetivo desenvolver um hidrogel inteligente, sensível a espécies reativas de oxigénio (ROS), que se encontram frequentemente em elevadas concentrações neste tipo de feridas, para permitir a libertação controlada de agentes antibacterianos. A metilcelulose (MC) foi escolhida como matriz do hidrogel devido à sua sensibilidade a ROS. No hidrogel foram incorporados dois compostos bioativos: (i) um péptido antimicrobiano (AMP, MSI78-Ahx-Cys), que atua na destruição das membranas bacterianas por contacto, e (ii) um oligonucleótido antissense (ASO) concebido para inibir a formação de biofilmes.

Os hidrogéis foram preparados com concentrações de MC a 6% e 8% e caracterizados por microscopia eletrónica de varrimento (SEM) e análise reológica. Foram avaliadas a temperatura de gelificação e as propriedades mecânicas. A temperatura de gelificação observada foi de ≈37ºC. Os hidrogéis com menor concentração (6% MC) demonstraram maior resistência à deformação do que os hidrogéis de 8% MC, que se revelaram mais quebradiços. A degradação por ROS foi induzida através de luz próxima do infravermelho (NIR-LED) e do fotoiniciador “indocyanine green”, demonstrando alterações estruturais e viscoelásticas consistentes com a degradação mediada por ROS.

Para melhorar a estabilidade do AMP face à degradação por proteases, o péptido foi imobilizado em nanopartículas de PLGA-PEG (AMP-NP). Estas nanopartículas foram sintetizadas por nanoprecipitação, apresentando tamanhos médios de 109 ± 1 nm (NP sem AMP) e 182 ± 2 nm (AMP-NP), com potenciais zeta de -4,6 ± 0,3 mV e -0,2 ± 0,2 mV, respetivamente. As AMP-NP mostraram eficácia contra *P. aeruginosa*, com uma concentração inibitória mínima (MIC) de 64 µg/mL e uma concentração bactericida mínima (MBC) ≥ 128 µg/mL. No entanto, a sua atividade foi inferior à do péptido livre (MIC = 8–16 µg/mL; MBC = 8–32 µg/mL).

ASOs com marcador fluorescente (Cy3-ASOs) foram usados para avaliar a capacidade do hidrogel em reter compostos de pequena dimensão na ausência de ROS. Os resultados mostraram libertação passiva dos Cy3-ASOs nas primeiras 24 h, independentemente da presença de ROS, indicando que os hidrogéis de MC não são adequados como sistemas inteligentes de libertação para pequenas moléculas como os ASOs. Em contraste, a libertação de nanopartículas foi significativamente aumentada

na presença de ROS. Notavelmente, os hidrogéis de 8% MC apresentaram um aumento de 37% na libertação de NP sob exposição a ROS, em comparação com condições sem ROS.

Em suma, os resultados indicam que os hidrogéis de MC são promissores como sistemas inteligentes de libertação capazes de disponibilizar nanopartículas bactericidas (AMP-NP) em resposta a ROS endógenas, oferecendo uma potencial estratégia para o tratamento de infeções bacterianas em feridas crónicas.

Palavras-chave: Hidrogéis; sistemas inteligentes de libertação; antimicrobianos; péptidos antimicrobianos; oligonucleótidos antissense; nanopartículas; feridas crónicas; espécies reativas de oxigénio.

Abstract

Chronic wounds represent a significant clinical challenge due to sustained inflammation and recurrent bacterial infections, particularly by *Pseudomonas aeruginosa* and *Staphylococcus aureus*. This study aims to develop a smart hydrogel responsive to reactive oxygen species (ROS), commonly elevated in such wounds, to enable controlled release of antibacterial agents. Methylcellulose (MC) was chosen as the hydrogel matrix due to its ROS sensitivity. Two bioactive compounds were incorporated: (i) an antimicrobial peptide (AMP, MSI78-Ahx-Cys), which disrupts bacterial membranes, and (ii) an antisense oligonucleotide (ASO) designed to inhibit biofilm formation.

Hydrogels were prepared at 6% and 8% MC concentrations and characterized by scanning electron microscopy (SEM) and rheological analysis. Gelation temperature and mechanical properties were evaluated. Gelation temperature suggested was ≈37ºC. Lower-concentration hydrogels (6% MC) showed greater resistance to deformation than the more brittle 8% MC hydrogels. ROS-responsive degradation was triggered using near-infrared light (NIR-LED) and the photosensitizer indocyanine green (ICG), showing structural and viscoelastic changes consistent with ROS-mediated breakdown.

To improve AMP stability against proteases, AMP was grafted onto PLGA-PEG nanoparticles (AMP-NP). These nanoparticles were synthesized by nanoprecipitation, showing average sizes of 109 ± 1 nm (bare NP) and 182 ± 2 nm (AMP-NP), with zeta potentials of -4.6 ± 0.3 mV and -0.2 ± 0.2 mV, respectively. AMP-NP were effective against *P. aeruginosa* exhibiting a minimal inhibitory concentration (MIC) of 64 µg/mL and minimal bactericidal concentration (MBC) of ≥ 128 µg/mL). However, their activity was reduced compared to free (MIC = 8–16 µg/mL; MBC = 8–32 µg/mL).

Fluorescently labelled ASOs (Cy3-ASOs) were used to evaluate the hydrogel capacity to retain small compounds in the absence of ROS. Results showed passive release of Cys-ASOs within 24 h, independent of ROS presence, indicating that MC hydrogels are not suitable as smart delivery systems for small molecules like ASOs. In contrast, nanoparticle release was significantly enhanced in the presence of ROS. Notably, 8% MC hydrogels exhibited a 37% increase in NP release under ROS exposure compared to non-ROS conditions.

Overall, the results indicate that MC hydrogels are promising smart delivery systems capable of releasing bactericidal nanoparticles (AMP-NP) in response to an endogenous ROS, offering a potential strategy to treat bacterial infections in chronic wounds.

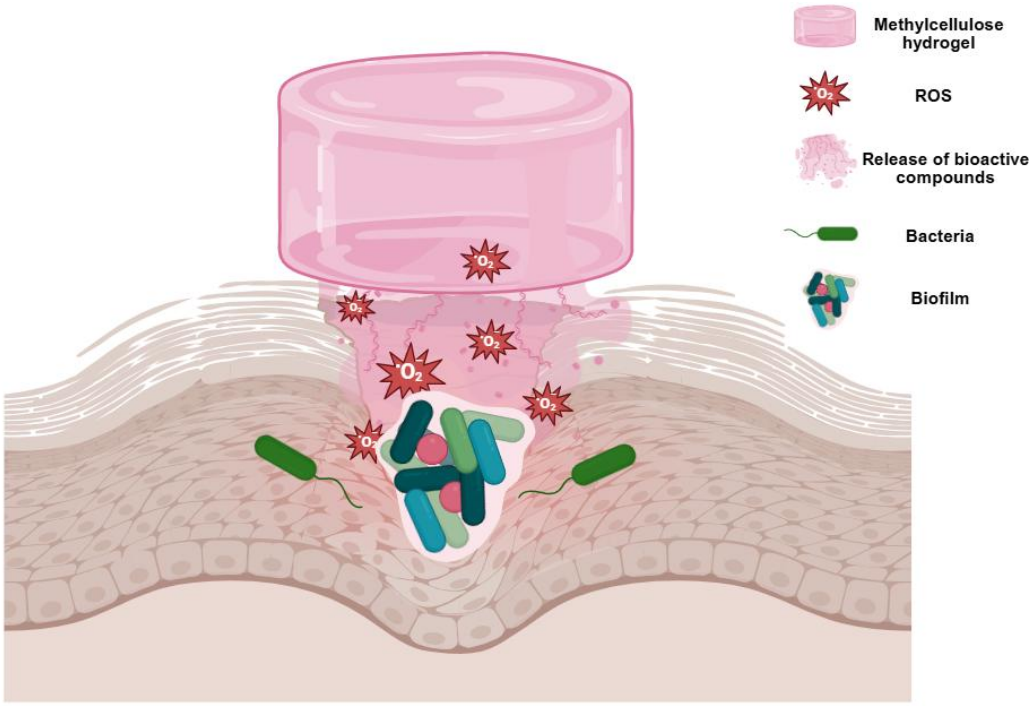


Figure 1- Schematic representation of the methylcellulose smart delivery hydrogel. Produced using BioRender software (https://www.biorender.com/)

Keywords: Hydrogels; smart delivery systems; antimicrobials; antimicrobial peptides; oligonucleotides, nanoparticles; chronic wounds; reactive oxygen species.

Index

Acknowledgements iii
Resumo vi
Abstract viii
List of Tables xiv
List of Figures xv
List of Abbreviations xix
Introduction 1
1. Skin wounds - overview 1
1.1 Wound healing 1
1.1.1 Typical wound healing 1
1.1.2 Chronic wounds (CW) 2
1.2 Bacterial infection 4
2. Emerging therapies 6
2.1 Wound-care dressings 6
2.1.1 Smart responsive polymer-based dressings 6
2.2 Methylcellulose 7
2.2.1 Rheological properties 9
2.2.2 ROS degradation 10
2.3 Bioactive compounds to prevent/fight biofilms 11
2.3.1. Antisense Oligonucleotides (ASOs) 11
2.3.2. Antimicrobial Peptides (AMP) 12
MSI78 (Pexiganan) 13
2.4 Nanoparticles (NP) 14
2.4.1 PLGA-PEG nanoparticles 15
..... 16
Aim 17
Materials and Methods 18

1. Nanoparticles (NP) production 18
1.1 PLGA-PEG NPs 18
1.2 Fluorescent PLGA-PEG NPs 18
1.3 PLGA-PEG-Mal NPs and AMP immobilization 18
1.4 NPs characterization 19
1.4.1 AMP quantification 19
2. Antimicrobial activity 20
3. ROS production 21
3.1 ROS production evaluation 21
4. Methylcellulose (MC) hydrogels 21
4.1 Scanning Electron Microscopy (SEM) 22
4.2 Rheological properties evaluation 22
5. Release assays 23
5.1 ASOs release and quantification 23
5.2 NPs release and quantification 23
5.2.1 ROS-induced release 23
5.2.2 Release of Bare-NPs 24
6. Statistical analysis 24
Results and discussion 24
1. Antimicrobial nanoparticles (AMP-NP) 24
1.1 AMP-NPs characterization 24
2. AMP-NP antimicrobial activity 26
3. ROS production evaluation 27
4. Methylcellulose (MC) hydrogel 28
4.1 Rheological properties evaluation 29
4.1.1 Gelation temperature determination 29
4.1.2 MC hydrogel mechanical properties 31
4.1.3 ROS influence in MC hydrogels mechanical properties 32
4.2 MC hydrogels morphology 34

5. Release assay 36
5.1 ASOs release from MC hydrogels 36
5.2 NP release from MC hydrogels 38
5.2.1 NP distribution into the MC hydrogel 38
5.2.2 Effect of ROS on NP release from MC hydrogels 39
6. General conclusions and future work 41
7. References 44

List of Tables

Table 1- Compilation of the characterization of every PLGA-PEG NP formulation through DLS and ELS (these are the results from 3 independent assays, with 3 replicates each): AMP-NP (AMP grafted onto PLGA-PEG-Mal-NP). bNP (bare PLGA-PEG-NP). Fluorescent bNP (FKR560 bare PLGA-PEG-NP); Both AMP-NPs and Fluorescent bNP are exclusively compared (statistically) with bNP using t-test; Statistically significant differences are indicated as *p < 0.05 and ns (not significant)..... 25

Table 2- Antimicrobial activity of AMP (MSI78-Ahx-Cys) and AMP-NP (MSI78-grafted onto PLGA-PEG-Mal-NPs). Minimal Inhibitory concentration (MIC) and Minimal bactericidal concentration (MBC) values expressed in µg/mL. These values are a result of 2 independent experiments with 3 replicates for free AMP and 1 experiment with 3 replicates for AMP-NP. 27

List of Figures

Figure 1- Schematic representation of the objective. Produced using BioRender software (https://www.biorender.com/) ix

Figure 2- Healing stages of chronic wounds. Image from [7]..... 1

Figure 3-Chronic wounds often have high levels of inflammation, harmful molecules like ROS and enzymes that break down tissue. They also tend to stay infected, and the cells do not respond well to healing signals. These wounds release a lot of exudates that contain enzymes like metalloproteinases (MMPs) and elastase, which damage healthy tissue around the wound. Because of all these problems, inflammation continues, and the wound has trouble forming new blood vessels and skin. Image from [8]. 4

Figure 4-Biofilm formation begins when environmental conditions trigger planktonic bacteria to attach to a surface using their adhesion structures. Through quorum sensing, the bacteria communicate and increase production of an extracellular matrix, while also altering their metabolism. This process firmly anchors the biofilm to the surface and helps protect the bacterial community from threats like antiseptics, ROS, and antibiotics. [31] 5

Figure 5-Examples of endogenous and exogenous stimuli for trigger smart release of therapeutic compounds. The top half represent the internal stimuli that are produced naturally in the biological environment (wound for example). The bottom half represents the external stimuli, provided, by a synthetic source, which can trigger or enhance the release of the compounds. Adapted from [89]..... 7

Figure 6- Chemical structure of anhydro-D-glucose monomers. These monomers form long chains when repeated. In cellulose, the R groups always correspond to hydrogen (H) radical, while in methylcellulose, the R group can be either H or methyl (CH_3) radicals at carbons 2, 3 and/or 6 of the glucose unit.[90]..... 8

Figure 7- Visual explanation of hydrogel transition in aqueous solution. MC fibres behaviour (interaction with water molecules) depending on temperature (low at left, high at right). At low temperatures, non-methylated regions of MC fibres stablish hydrogen bounds with water molecules in the medium, forming one phase. When the temperature is higher, those bounds break, and the polymer forms hydrophobic globules. This

transition forms the separation of two phases, one hydrophobic, which is the polymer and the other which is water. Adapted from [43]. 9

Figure 8- Demonstration of gene knockout mechanism of ASOs. Scheme produced via BioRender software (https://www.biorender.com/). 12

Figure 9- Main modes of action of soluble AMP: carpet, barrel stave and toroidal pore model. [67] 13

Figure 10- Amino acid distribution in α-helical structured MSI78. Image from [69]. 14

Figure 11- Representation of the thiol-maleimide reaction between PLGA-PEG-Mal and cysteine-modified AMP (AMP-Ahx-Cys). Mal: maleimide group; Ahx: 6-aminohexanoic acid ; Cys: cysteine amino acid . Adapted from [81]. 15

Figure 12- Representation of the chemical structure of PLGA-PEG copolymer. PLGA: poly(D,L-lactide-co-glycolide); PEG: polyethylene glycol; LA: lactic acid monomer; GA: glycolic acid monomer. Adapted from [91] 16

Figure 13- In house NIR-LED system produced by P.Alves [83], fitting 6-well plates, used to produce ROS. 21

Figure 14- Quantification of ROS-triggered conversion of DPBF to a compound non-detectable at 410nm, in two tested conditions when NIR was ON and OFF. These are the results of two independent assays with 3 replicates each. Statistically significant differences are indicated as *p < 0.05; **p < 0.01; ***p < 0.001 and ns (not significant). 28

Figure 15- Gel transition from a transparent solution (left) and the formation of the hydrogel (right), which turns turbid and keeps the format of the Eppendorf tube if pulled out. 29

Figure 16- Variation of G'' and G' of 8% MC solutions upon heating, according to different angular frequencies. On the left it is possible to see the variation of temperature on G''. On the left it is possible to see the influence of temperature in G', showing frequency dependence at lower temperature and losing that dependency at higher temperatures. This is a result of 1 independent assay. 30

Figure 17- Variation of tan δ of 8% MC solutions upon heating, according to different angular frequencies. The left graphic shows the entire data for 3 angular frequencies tested (1,3 and 7 Hz), where is possible to see the intersection point. On the right graphic it is possible to see the intersection of the curves between 37 and 37.5ºC. This is a result of 1 independent assay. 31

Figure 18- Resulting graphics from the amplitude sweep assay. Graphs 1 and 3 represent the mechanical properties of 6% (w/v) MC hydrogel, while graphs 2 and 4 correspond to the 8% (w/v) MC hydrogel. Graphs 3 and 4 display the full-scale data for both hydrogels. The dark circles on graphs 3 and 4 highlight the LVER region, which is zoomed in on graphs 1 and 2 on the left. Results for both conditions are based on 3 independent assays. Statistically significant differences are indicated as *p < 0.05; **p < 0.01; ***p < 0.001, ****p< 0.0001 and ns (not significant) determined by t-test. 32

Figure 19- Resulting graphics from the amplitude sweep assay showing the influence of ROS in G' and G'' of MC hydrogels (6% and 8%) within the LVER region. These graphs represent data from one independent assay. Statistically significant differences are indicated as *p < 0.05; **p < 0.01; ***p < 0.001, ****p< 0.0001 and ns (not significant). Comparisons were made only between NIR ON and NIR OFF for each concentration using the t-test. 33

Figure 20- SEM images comparing 8% MC hydrogel (two images on the left) with 6%MC hydrogel (two images on the right. For both conditions the scales are represented on the bottom. Only 50 µm and 30 µm scales were compared for all the images taken. Images from 8% MC were taken of a portion of the surface of the hydrogel, instead of cross-section, due to difficulties on identifying the cross-section site of the samples after freeze-dried. 35

Figure 21- SEM images comparing 8%MC hydrogels when the NIR are OFF (two images on the left) with when the NIR are ON (two images on the right. In the 8% NIR ON image (30 µm) it is possible to see fine fibres from deeper layers, as described in the text, which is not seen in the 8% NIR OFF corresponding image. For both conditions the scales are represented on the bottom. Only 50 µm and 30 µm scales were compared for all the images taken. Images from 8% NIR ON were taken of a portion of the surface of the hydrogel, instead of cross-section, due to difficulties on identifying the cross-section site of the samples after freeze-dried. 36

Figure 22- ASOs release profile in different MC hydrogels (6,7 and 8% w/v). Every sample was compared to MC hydrogel without ASOs. For each concentration, the results shown are the result of 3 independent assays. Deviation between replicates is represented in all the graphics, although cannot be clearly seen in 6 and 7%, since it is so low. 37

Figure 23- NP distribution profile in 8% MC hydrogel visualized by confocal microscopy. A schematic diagram at the top right of the figure view that indicates the hydrogel regions corresponding to each confocal image (A, B, and C). Red signals represent the

fluorophore incorporated in PLGA-PEG-FKR560 NPs (30%). The isolated image at right shows the control hydrogel (without fluorescent PLGA-PEG NPs). 39

Figure 24- NPs release from the hydrogel after 24h. The results shown are the cumulative of timepoint 0h,1h and 24h, originated by 2 independent experiments: The total amount of NPs released for both concentrations is very low in comparison to the initial concentration of NPs included in the hydrogel (3.2e12 NP/mL); It is possible to see clear differences between samples with and without ROS (NIR ON vs NIR OFF), specially at 8% MC. Statistically significant differences are indicated as *p < 0.05; **p < 0.01; ***p < 0.001 and ns (not significant). 40

List of Abbreviations

$^1O_2$	Singlet oxygen
Ag	Silver
Ahx	6-aminohexanoic acid
AMP	Antimicrobial Peptide
AMP-NP	Antimicrobial Peptide-loaded Nanoparticle
ASO	Antisense Oligonucleotides
Au	Gold
bNP	Bare Nanoparticle
BSA	Bovine serum albumin
CFU	Colony Forming Unit
CH3	Methyl radicals
Cp	Centipoise
CuO	Copper oxide
CW	Chronic Wound / Chronic Wounds
Cys	Cysteine
DLS	Dynamic Light Scattering
DNA	Deoxyribonucleic acid
DPBF	1,3- diphenylisobenzofuran
DS	Degree of Substitution
ECM	Extracellular Matrix
ELS	Electrophoretic Light Scattering
FCUP	Faculdade de Ciências da Universidade do Porto
FDA	Food and Drug Administration
FDA	Food and Drug Administration
G'	Elastic module
G''	Viscous module
GF	Growth Factors
H	Hydrogen radicals
Hz	Hertz
ICG	Indocyanine Green
IE%	Immobilization Efficiency (percentage)
LCST	Lower Critical Solution Temperature
LED	Light-emitting diode
LVER	Linear viscoelastic region
Mal	Maleimide group
MBC	Minimum Bactericidal Concentration
MC	Methylcellulose
MHB	Mueller–Hinton Broth
MIC	Minimum Inhibitory Concentration
mRNA	Messenger RNA

mV	Millivolts
MW	Molecular Weight
NaCl	Sodium Chloride
NIR	Near Infrared
nm	Nanometres
NMWL	Nominal molecular weight limit
NP	Nanoparticles
NTA	Nanoparticle tracking analysis
OD	Optical Density
PBS	Phosphate Buffered Saline
PdI	Polydispersity Index
PEG	Polyethylene Glycol
PGA	Poly glycolic acid
PLA	Poly lactic acid
PLGA	Poly(D,L-lactide-co-glycolide)
PLGA-PEG	Poly(D,L-lactide-co-glycolide) polyethylene glycol
ROS	Reactive Oxygen Species
SDF-1	Stromal derived factor
SEM	Scanning Electron Microscopy
SH	Thiol group
TG	Gelation Temperature
TiO_2	Titanium dioxide
TSA	Tryptic soy agar
TSB	Tryptic Soy Broth
UP	University of Porto
ZnO	Zinc oxide
δ	Phase angle

Introduction

1. Skin wounds - overview

The skin, the largest organ present in the human body, is the main source of protection of the organism against the adversities of the environment such as bacteria, xenobiotics and dehydration[1]. Also, in everyday life, this barrier is subjected to a variety of damages which may lead to extensive wounds [2], [3]. Skin wound closure can be processed by tissue regeneration, which means that the damaged tissue can be replaced by new tissue (mucosa, epidermis, etc), or most commonly, by tissue repair, where there is the formation of a scar and fibrotic tissue.

1.1 Wound healing

1.1.1 Typical wound healing

In both cases, wound healing process is proportionated by a very complex “orchestra” that combines the action of cells, growth factors (GF) and cytokines [4], that can be divided into 4 different stages: haemostasis, inflammation, proliferation and remodelling. (Figure 2)

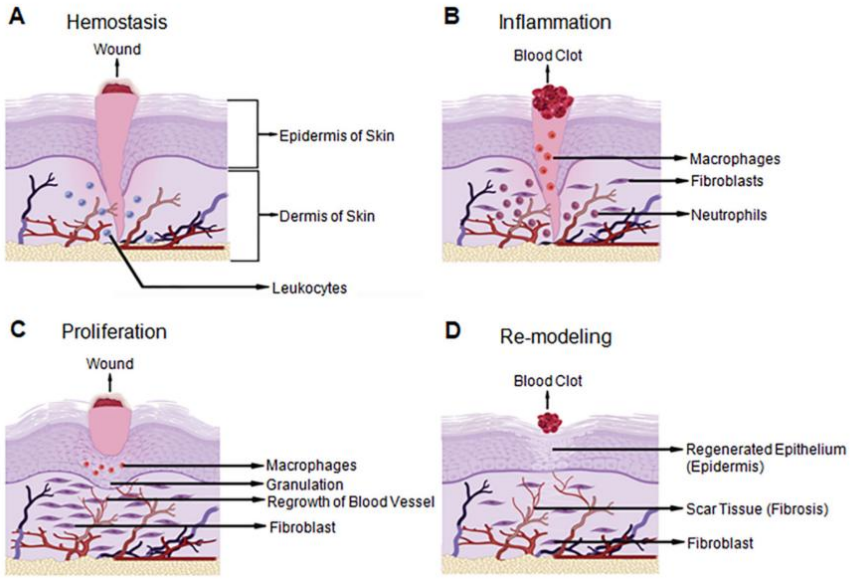


Figure 2- Healing stages of chronic wounds. Image from [7]

In the initial phase (haemostasis), vasoconstriction and the formation of a blood clot, impede the blood loss, creating a temporary barrier that protects the wound site and allows the migration of inflammatory agents and resident skin cells, which promote the healing of the wound [5], [6], [7]. Then, in the inflammatory stage, there is a vasodilation of the local capillaries that increases the recruitment of leukocytes to prevent infection. Also, pro-inflammatory cytokines and growth factors are released on to the wound site to stimulate leukocytes maturation and tissue regeneration. In this context, neutrophils protect the wound from microorganisms, by generating reactive oxygen species (ROS), releasing proteases and antimicrobial peptides (AMP), and clear the debris of the wound [7]. In proliferation, there is the formation of granulated tissue, which is composed of extracellular matrix (ECM), connective tissue and new blood vessels, that will reduce the size of the wound. This stimulation is possible due to the high concentrations of cytokines and growth factors that ensure ECM production, by fibroblasts, and keratinocyte proliferation, culminating in the formation of new tissue. This phase ends with the formation of granulated tissue, rich in fibroblasts, macrophages, capillaries and loosely organized collagen bundles [5], [6], [7]. The remodulation of the tissue can extend over 1 year and it's characterized by decreasing of cellularity, vasculature and the transformation of the granulated tissue into a scar. This process can be compromised by some insults to that region, which can deregulate the imbalance of matrix metalloproteinases and inhibitors, resulting in the formation of keloids and hypertrophic scars, characterised for excessive ECM components, that decrease the elastic characteristic of the skin, or even the formation of more serious injuries [5], [6].

1.1.2 Chronic wounds (CW)

If these topical injuries are associated to extreme difficulties in regeneration, they are known as chronic wounds (CW). Generally, chronic wounds stay in a self-perpetuating inflammatory stage, associated with impaired angiogenesis, difficult re-epithelization, imbalance of cytokines/ GF and increased protease activity [8].

It is estimated that 1-2% of the population in developed countries will suffer from CW during their lifetime. With increasing levels of elderly worldwide, populations start to show increasing numbers of diabetic and obese patients, which are indirectly related to CW development. These pathologies decrease the regeneration capacity of the tissues, needing more than 12 weeks to fully heal [9], [10]. In these situations, neutrophils exhibit abnormal phenotypes and lose important functions. Additionally, there is reduced macrophages activated in M2 profile (with anti-inflammatory and tissue repairing

functions) and lower antimicrobial activity [11], [12]. It is well known that wound closure depends on M2 macrophages. The reduced activity of these cells in diabetic chronic wounds, for example, is due to the impairment transition from M1 (pro-inflammatory macrophages) to M2, caused by excessive glycation end products (AGEs) [13]. In the context of obesity, an excess of adipose tissue also inhibits M2 macrophages polarization [14].

Additionally, some studies suggest that keratinocytes present in CWs exhibit impaired migratory potential due to their hyperproliferative behaviour which incapacitates them from migrating and helping in wound closure. Also, there is a notable loss of response from the fibroblasts that show significantly less expression of GF receptors, as well as decreased phosphorylation of key signalling proteins [2], [15]. Not only, but also, in diabetic wounds, angiogenesis is impaired due to the poor response of endothelial progenitor cells to SDF-1(stromal derived factor), which impedes cell maturation and proliferation [16].

Other characteristics of CW include a higher pH value (>7.3 compared to the healthy value 5.5), which favours bacterial colonization and biofilm formation, as well as an increased temperature (from 32.6ºC to 35ºC). In addition, high concentrations of ROS and proteases perpetuate the inflammatory stage, damage wound tissue and delay the healing [1], [2], [17]. When present in low concentrations, ROS favour the wound healing and prevent microbial colonization, which are characteristics of typical/healthy wound healing. On the other hand, at high concentrations, ROS are related to oxidative stress and delay the wound healing process by degrading proteins from ECM and dermal fibroblast disfunction [18].

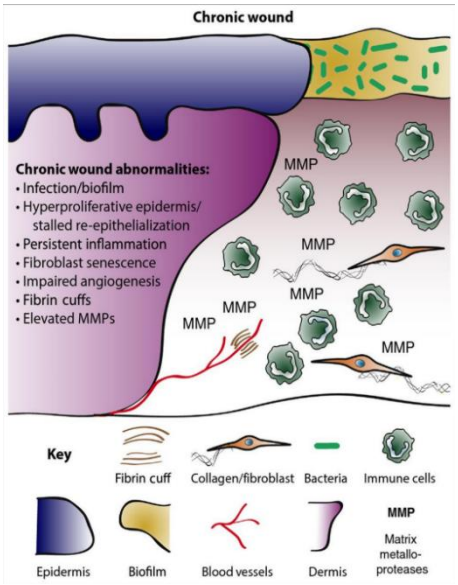


Figure 3-Chronic wounds often have high levels of inflammation, harmful molecules like ROS and enzymes that break down tissue. They also tend to stay infected, and the cells do not respond well to healing signals. These wounds release a lot of exudates that contain enzymes like metalloproteinases (MMPs) and elastase, which damage healthy tissue around the wound. Because of all these problems, inflammation continues, and the wound has trouble forming new blood vessels and skin. Image from [8].

1.2 Bacterial infection

Bacterial infections are very common in CW, due to high exposure to the atmosphere and the more neutral pH (>7.3), which favours microbial colonization.[19] The most common microorganisms found in CW are *Staphylococcus aureus* and *Pseudomonas aeruginosa,* Gram-positive and Gram-negative bacteria, respectively.[20] Also, there is an almost universal theory that *S. aureus* is found in every wound and *P. aeruginosa* is found in more than half of the infected wounds, predominantly in large wounds [21], [22]. These bacterial species produce destructive virulence factors that enhance their infectious capabilities and delay wound healing. In addition, they produce large amounts of extracellular compounds that contribute to biofilm formation [23].

Biofilm can be described as a three-dimensional matrix composed of bacteria embedded in a conglomeration of extracellular polymeric substances, which facilitate bacterial colonization of the wound tissue by supporting proliferation and providing protection from immune system and antimicrobial agents, such antibiotics (Figure 4) [23]. Bacteria can attach not only to biological tissues, but also to abiotic materials, like implants or prostheses. The initial attachment of this microorganisms is guaranteed by physicochemical and electrostatic interactions with the target tissue/material [23].

However, interaction with biological tissue requires specific receptor-ligand interactions because, both bacterial and cell barriers are negatively charged, which increases the repulsive electrostatic forces. For this reason, bacteria have had to develop targeted interactions to promote their successful attachment (*P.aeruginosa* use exopolysaccharides that complex to surface materials, like Pel, Psl, and alginate and/or several adhesins that are produced after biofilm formation to maintain the architecture and secure the attachment, like FliD, type IV pili, CdrA) [22], [24], [25], [26]. Also, a complex series of regulatory events that control gene expression and allow the transition from the planktonic stage to the biofilm phenotype, (provided by environmental stimulus like chemical and/or mechanical stimulus and quorum sensing) are responsible for the success of the colonization [27].

The widespread and “old-fashioned” use of antibiotics may become a major problem in the near future, due to the increasing numbers of antibiotic-resistant bacteria species. The majority, growing in biofilms, stay in dormant state, which, in parallel with biofilm matrix, protects them from the therapeutic agents (antibiotics) and immune cells [28]. Concerning bacteria-resistance, *P. aeruginosa* developed strategies that protects them against multiple classes of commonly used antibiotics, like *β*-lactams, aminoglycosides and fluoroquinolones [29]. In addition, the multidrug resistant strains of *S. aureus* that are, not only, highly resistant against methicillin, but also to other clinical used antibiotics such as tetracycline, ampicillin and oxacillin [30].

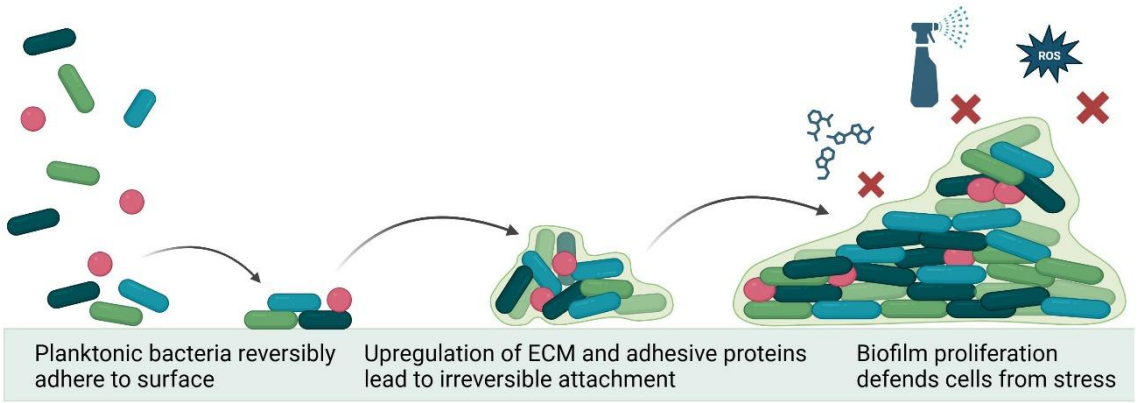


Figure 4-Biofilm formation begins when environmental conditions trigger planktonic bacteria to attach to a surface using their adhesion structures. Through quorum sensing, the bacteria communicate and increase production of an extracellular matrix, while also altering their metabolism. This process firmly anchors the biofilm to the surface and helps protect the bacterial community from threats like antiseptics, ROS, and antibiotics [31].

2. Emerging therapies

Right after the injury, it is important to remove potential barriers that impair the correct wound healing, which is called debridement. It is used to remove nonviable and infected tissue (biofilms), as well as excessive moisture. After that, the wound bed should be protected by applying temporary barriers, such as wound dressings, to preserve the optimal physiological conditions for wound healing.

2.1 Wound-care dressings

Wound dressings are regularly used in the treatment of chronic wounds. These dressings must protect the wound from infection, ensure comfort in its usage, keep a moisty environment and, of course, be non-toxic, non-adherent and non-irritant, preferentially, stimulating the regeneration of the tissue [32].

Wound dressings can be applied in different forms, such foams, hydrogels, films and others, depending on the location [33], [34]. However, there is a problem associated with the traditional wound dressings (wool dressings, plaster, gauze and bandages) which is their incapability of retaining the wound exudate, that leads to its leakage, increasing the chances of bacterial infections [35]. Accordingly, the development of advanced wound dressings is essential. These dressings should not only maintain optimal moisture levels within the wound bed but also prevent or combat infection and stimulate tissue regeneration through the use of smart drug delivery systems that release therapeutic compounds in response to intrinsic or extrinsic stimuli [2], [36].

2.1.1 Smart responsive polymer-based dressings

Polymers are frequently used to produce wound dressings. They can be divided in natural (produced from natural sources) and synthetic (chemically produced in laboratories). Certain polymers, such as carboxymethyl cellulose [37] and heparinised polyvinyl alcohol/chitosan [38] were explored as smart wound dressings for the delivery of therapeutic compounds in response to specific endogenous or exogenous stimulus [32]. Endogenous stimulus include temperature, reactive oxygen species (ROS), pH and enzyme activity, as these factors can differ significantly between infected and non-infected non-healing wounds. Exogenous stimulus commonly used include light, magnetic fields and heat (temperature), which are applied from external sources [2], [39].Some of the most commonly used endogenous and exogenous stimuli to trigger the smart release of therapeutic compounds are summarized in Figure 5

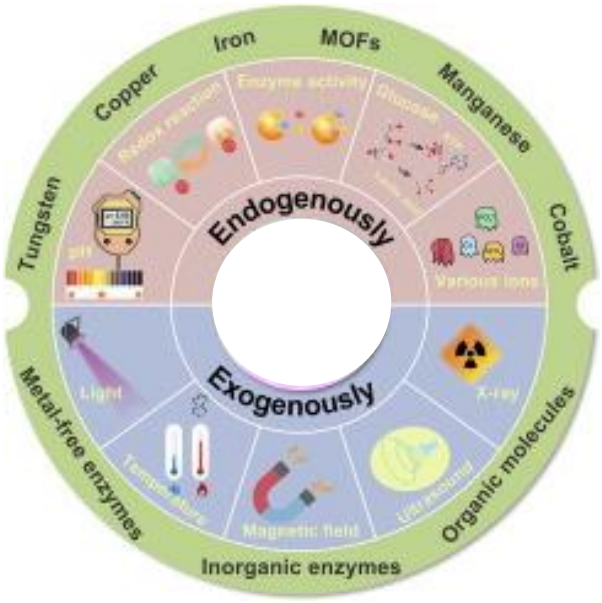


Figure 5-Examples of endogenous and exogenous stimuli for trigger smart release of therapeutic compounds. The top half represent the internal stimuli that are produced naturally in the biological environment (wound for example). The bottom half represents the external stimuli, provided, by a synthetic source, which can trigger or enhance the release of the compounds. Adapted from [87].

Some polymers are sensitive to more than one type of stimulus. For instance, methylcellulose exhibits both thermosensitivity and responsiveness to reactive oxygen species (ROS).

2.2 Methylcellulose

MC is a cellulose ether, very similar to conventional cellulose, but instead of hydroxyl groups (-OH) in C-2, C-3 and/or C-6 of the anhydro-D-glucose units, it may have methoxy groups ($-OCH_3$) (Figure 6) . These substitutions may be quantified by the degree of substitution (DS: 0-3) [40]. DS and molecular weight (MW) can interfere with some characteristics of the polymer like solubility in water (amphiphilic polymer) and the rheological properties, which are also dependent on the distribution of the methyl groups along the chains [40], [41].

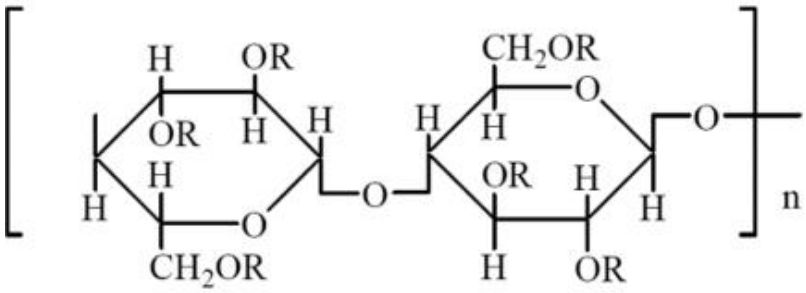


Figure 6- Chemical structure of anhydro-D-glucose monomers. These monomers form long chains when repeated. In cellulose, the R groups always correspond to hydrogen (H) radical, while in methylcellulose, the R group can be either H or methyl (CH_3) radicals at carbons 2, 3 and/or 6 of the glucose unit [88].

This water solubility is possible because its chains present high and low methylated regions, where the low methylated ones enable the formation of hydrogen bonds with water molecules present in the external medium. This process does not happen in common cellulose due to its crystalline and packed structure, which is caused by intra- and inter-molecular hydrogen bonds [41]. Due to MC water solubility and singular thermal behaviour, it is possible to produce thermo-reversible hydrogels using this polymer [42]. The hydrogel formation happens through changing from hydrophilic (MC solution) state to hydrophobic state (MC Hydrogel), based on hydrogen bonds, that are present between the polymer and surrounding water molecules at low temperatures, as already mentioned. Hence, the polymer chains are hydrated and solubilized resulting in a one-phase system. At increased temperature, the hydrogen bonds with water molecules brake, and the polymer chains cannot be solubilized anymore leading to polymer aggregation. In resume, at low temperatures, the polymer chains stay “comfortable” around water molecules, which is possible due to the low thermal energy of the system, enabling hydrogen bounds formation with water. Whereas, at high temperatures, the chains start to wrap on themselves, forming dehydrated globules, due to the high thermal energy of the system, which culminates in the hydrogel formation (Figure 7) [43].

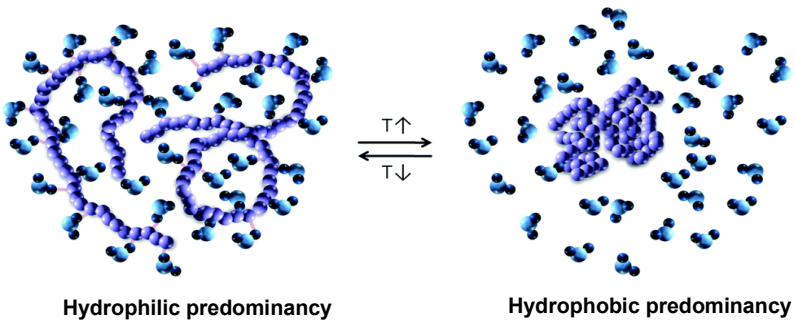


Figure 7- Visual explanation of hydrogel transition in aqueous solution. MC fibres behaviour (interaction with water molecules) depending on temperature (low at left, high at right). At low temperatures, non-methylated regions of MC fibres stablish hydrogen bounds with water molecules in the medium, forming one phase. When the temperature is higher, those bounds break, and the polymer forms hydrophobic globules. This transition forms the separation of two phases, one hydrophobic, which is the polymer and the other which is water. Adapted from [43].

2.2.1 Rheological properties

Since MC forms thermosensitive hydrogels, it is important to predict how it would behave in its real applications. Rheological studies can be used to obtain data from the effect of temperature and mechanical deformation on MC viscosity, stiffness and also, the gelation temperature. These data can be obtained using a rheometer that allows the study the deformation and flow behaviour of materials by applying mechanical tensions and temperature to samples [44].

MC is considered a viscoelastic material, which means it may exhibit both viscous and elastic behaviours, depending on deformation [45]. Knowing this, the rheometer, normally, works in oscillatory mode, in order to study the resistance of the hydrogel against shear strain.[44] The parameters that measure this mechanical behaviour are the elastic modulus (G'), the viscous modulus (G'') and phase angle (δ). The first two moduli form the linear viscoelastic region (LVER), which is the portion of the graphics, where both G' and G'' stay constant, when subjected to a range of mechanical stress, below a critical strain value.[46] Values of shear strain above that LVER will promote a transition from elastic state (solid like) to viscous (liquid like), which indicates that the hydrogel was not able to resist that deformation and broke. The δ is an angle value, that can be obtained in a sinusoidal function, which characterize the offset of shear strain and resulting shear stress. This angle varies between 0-90º. If the value is below 45º, the sample behaves like a solid at rest, but if it is higher than 45º, it behaves like a liquid at rest [44].

This kind of information can be important to predict how the hydrogel will behave when applied in a wound. For example, whether it drips or resists to shear forces applied to the wound site.

Other parameter that influences the mechanical behaviour of the hydrogel is the gelation temperature. Since the MC is thermo-responsive, understanding its transition from a solution to a hydrogel is essential for protocol optimization and to tunning this transition, when necessary.

As described, in the DS range from 1.4 to 2.0, a transition from a solution to a hydrogel can be observed upon heating and a reverse transition from gel to solution occurs upon cooling [47]. Depending on the MC concentration in an aqueous solution, above a critical temperature point (LCST), its viscosity increases significantly over time with temperature. At room temperature, it remains a highly viscous transparent solution, often referred as a pre-gel. When the temperature reaches a specific value, referred to as the gelation temperature (T_G), there is a phase separation leading to the formation of a turbid and strong hydrogel [40]. This phase transition can also be monitoring by observing the evolution of the variables previously described (G', G'', and δ) as the temperature increases [48].

Both stiffness and $T_{G,}$ can be tuned by adjusting the concentrations of the compounds used in hydrogel preparation, such as polymer concentration, salt concentrations (PBS), viscosity and the molecular weight of the MC, in order to obtain a hydrogel that suits the specific needs [40].

2.2.2 ROS degradation

ROS-responsive smart drug delivery systems have been explored due to the elevated levels of ROS associated with a specific stage of wound healing (inflammatory phase), particularly in infected chronic skin wounds [49], [50]. Some examples of ROS-sensitive biomaterials include poly(propylene-sulfide), boronic esters, and poly(thioketal), which have been used in the treatment of neurodegenerative diseases and infected chronic wounds, conditions characterized by high oxidative stress and elevated level of ROS, such as hydrogen peroxide, hydroxyl radicals, superoxide anions [51], [52], [53].

In the case of MC, the release triggered by ROS was inspired by a natural process. Brown-rot fungi produce a non-enzymatic cocktail, rich in ROS, that degrades cellulose present in wood cell wall [50]. ROS, like singlet oxygen ($^1O_2$) for example, is described as capable of decrease MC viscosity 30-50%, suggesting the degradation of its chains [54]. This makes MC a great polymer to be used as a smart delivery hydrogel, releasing the bioactive molecules in response to an endogenous stimulus (ROS produced in infected chronic wounds) slowly and controlled in time. This strategy was recently used in a different context to release doxorubicin (a chemotherapeutic drug) from cellulose microparticles, using an artificial ROS generating assay [55]. ROS can be easily

generated in the laboratory by applying a near-infrared (NIR) laser onto an FDA-approved photosensitizer, indocyanine green (ICG) [55]. This strategy enables the development of ROS-sensitive drug delivery systems by mimetite the ROS present in infected wounds.

2.3 Bioactive compounds to prevent/fight biofilms

In a first instance, after the wound debridement, the approach should be the release of therapeutic compounds in order to impede or decrease the formation of biofilms, since it is the major problem in chronic infections, protecting the bacteria from the immune system and antibiotics. By slowing down biofilm formation, it is easier to kill bacteria with antibiotics, for example. On the other hand, it is important to use alternatives to common antibiotics, to reduce chances of creating multiple resistant bacteria and still eradicate bacteria. There is a variety of bioactive compounds described in literature that have shown to be good candidates for potential therapies in this field. Good examples of this therapeutic agents are the Antisense Oligonucleotides (ASO), that can be used for inhibiting biofilm formation (gene therapy) and the Antimicrobial Peptides (AMP) which can kill bacteria, in low doses, by contact with cell membranes.

2.3.1. Antisense Oligonucleotides (ASOs)

ASOs are short nucleic acid oligomers (10-20 bases) that show promise in drug therapy, as they act as knock out agents that can repress the expression of any gene of interest. They are generally used to target mRNA sequences, interrupting or not allowing, the translation of that specific sequence, which repress the expression of the associated gene [56]. The mechanism used is very well studied (Figure 8), the binding of the oligonucleotides to the target sequence happens via Watson-Crick base pairing and this hybridization can block mRNA translation by not allowing the ribosome binding, which stops or impedes the translation process, or even by degradation of the hybrid molecule, by degradative enzymes like RNAse-H [57].

Although these therapeutics have shown good results in cancer treatment, for example, they lack on efficiency when subjected to nucleases, poor penetration across membranes and non-optimal target affinity. For these reasons, some modifications can be introduced in the oligonucleotide molecule to facilitate and enhance its features [57],[58]. Although some modifications in the nucleic acids can interfere with their resistance against degradation and increase their hydrophobicity, they are still inefficient

in penetrating inside negatively charged membranes by themselves, due to their short lengths and low charge density [57]. One of the strategies used for their transfection is to immobilize them on to nanoparticles surfaces (gold nanoparticles as example), using thiolated oligonucleotides dispersed in dens monolayer [59]. It was already proved that these conjugations are highly resistant to degradation, increase the binding of the oligonucleotides towards the target and allow the transfection [60]. Also it is important to know that there was already proposed that the conjugation of the nucleic acids and peptides on nanoparticles surface would also be possible as synergic therapies [60], [61].

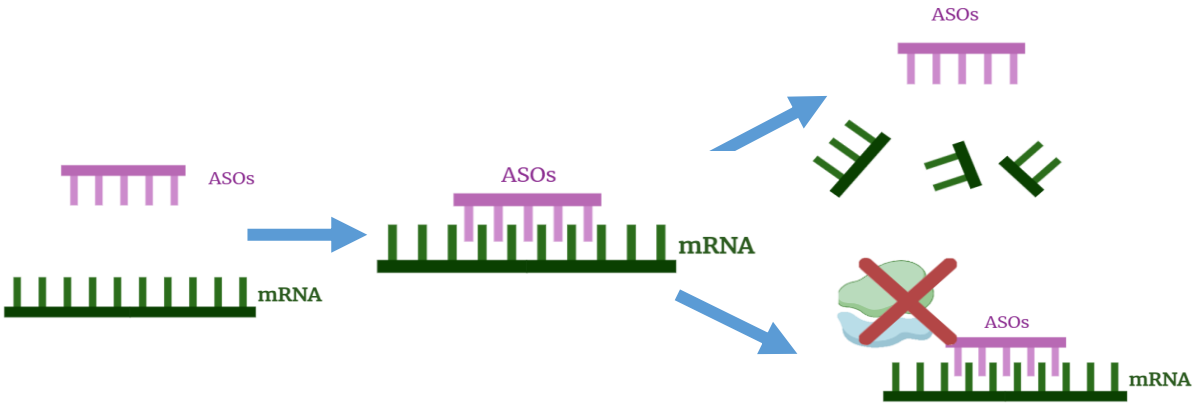


Figure 8- Demonstration of gene knockout mechanism of ASOs. Scheme produced via BioRender software (https://www.biorender.com/).

2.3.2. Antimicrobial Peptides (AMP)

Antimicrobial peptides (AMP) are typically short amino acid sequences, usually ranging from 10 to 50 residues. They are amphiphilic in nature and carry a net positive charge. Their secondary structure, most commonly in the form of α-helix, plays a crucial role in their antimicrobial activity [62], [63]. They have broad-spectrum antimicrobial activity, mainly against a wide range of bacterial species. Their overall positive charge is attracted to the negatively charged bacterial membranes, and their hydrophobic portion helps their insertion and translocation into the membranes, causing membrane disruption and pores formation, which leads to cell lyses and death [64], [65]. This mechanism of action impedes resistance development in bacteria and enhances their potential as antimicrobial agents for treating infection [66]. Moreover, this electrostatic interaction mechanism allows AMP to selectively target bacterial membranes, which have a more negative charge compared to mammalian cells. The specific AMP antimicrobial interactions depend only on its specific properties. There are three main mechanisms of

action: the carpet model, the barrel stave model and the toroidal pore model (Figure 9) [67].

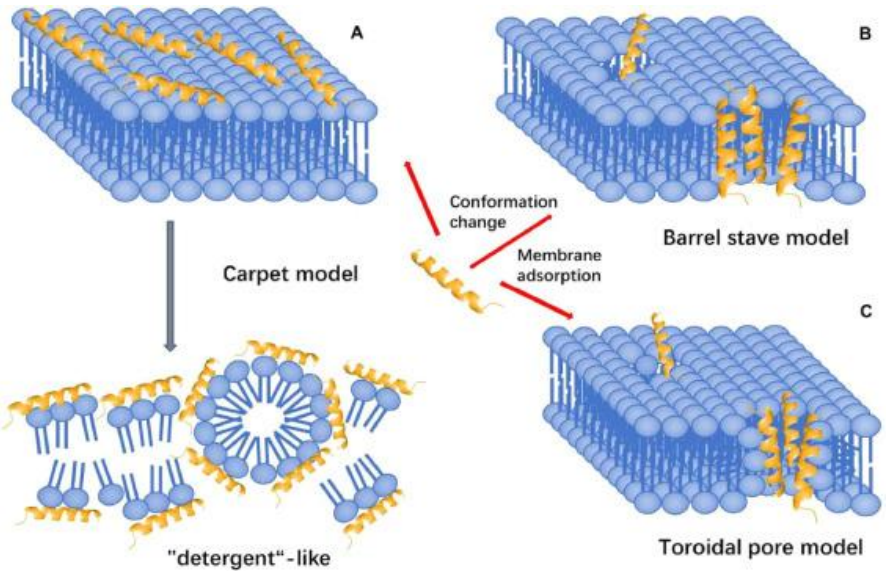


Figure 9- Main modes of action of soluble AMP: carpet, barrel stave and toroidal pore model [67].

However, due to their protein nature, AMPs are always susceptible to enzymatic degradation, which often occurs in infected chronic wounds.[8] AMP immobilization onto biomaterials, namely nanoparticles (NPs), has emerged as promising strategy explored by several researchers to overcome this problem. This approach protects AMP from proteases degradation, probably due steric hindrance, while maintaining their antimicrobial activity [64].

MSI78 (Pexiganan)

Pexiganan (MSI78), one of the most well-known AMPs, was the peptide explored in this work due to its broad spectrum of activity, even against multidrug-resistant bacteria and its low propensity to induce bacteria resistance [68]. Moreover, MSI78 is one of the most well-characterized AMP. It is composed by 22 amino acids (GIGKFLKKAKKFGKAFVKILKK), which adopted an α-helical structure, upon contact with bacterial membranes, exposing hydrophilic amino acids in one side and hydrophobic amino acids on the other (Figure 10). The hydrophilic amino acids, mainly, lysine residues, are responsible for the AMP cationic nature, which enables electrostatic interactions with the anionic bacterial membranes. The hydrophobic amino acids

(phenylalanine, valine, leucine and isoleucine) are important for the AMP translocation through the lipidic membranes of bacteria, leading to their disruption [69]. Also, other residues like alanine are important to increase the α-helix stability [68].

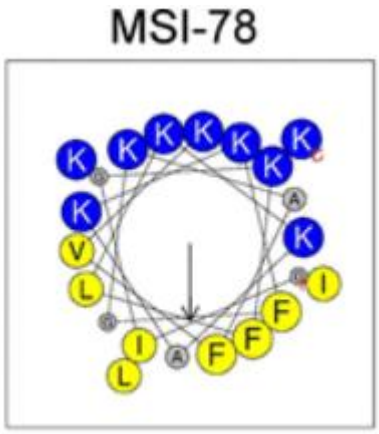


Figure 10- Amino acid distribution in α-helical structured MSI78. Image from [69].

MSI78 is known to form dimers stabilized through hydrophobic interactions. Its mechanism of action involves the disruption of bacterial membranes by forming toroidal-type pores. As one of the most well-characterized and effective antimicrobial peptides, MSI78 has been extensively studied [68].

2.4 Nanoparticles (NP)

Nanoparticles (NP) have been more and more used in the development of new therapeutics and disease diagnostics, showing high potential to alter biological events, like infections [70]. Their small sizes (1-100 nm) allow easy uptake by cells [71]. Metal and metal oxides NPs have been explored in the treatment of chronic skin wounds infections due to their ability to fight multi-drug-resistant bacteria and penetrate the strongest biofilms [72]. However, their use raises safety concerns that need to be carefully addressed. Some examples that raise warnings about the use of these type of NPs includes ZnO and TiO_2, which can damage DNA; CuO which can cause oxidative lesions; and the well-known Ag and Au NP, used in medical treatments/diagnosis, but which can accumulated in vital organs such as liver, lungs and spleen, posing the risk of potential organ damage.[73], [74], [75] On the other hand, polymeric and lipidic NP are suggested to be an excellent alternative to metal-based NPs due to their biocompatibility and degradability [76], [77].

These NP can be used not only as biological modulators themselves, containing polymers with some antimicrobial activity, such as chitosan, but also as carriers for the delivery of therapeutic compounds, like AMPs and ASOs [76], [78], [79].

As already mentioned, compounds like ASOs and AMPs can be immobilized on NPs surface to avoid nuclease/protease degradation increasing their stability in physiological environments. ASOs / AMP surface immobilization can be achieved through maleimide-thiol covalent interaction under mild reactions, at neutral pH, and in aqueous media at room temperature, making the process safer, user-friendly and highly effective. Maleimide (Mal) functional groups exhibit high chemical selectivity toward thiol groups (-SH), which are present either in modified nucleic acid (thiol-ASO) or in cysteine amino acid, that can be included into the AMP, thereby enabling control over the ASOs and AMP surface orientation (Figure 11). In addition, the spacer 6-aminohexanoic acid (Ahx) is commonly inserted between cysteine and the AMP moiety (AMP-Ahx-Cys) to improve molecular flexibility and reduce steric hindrance thereby facilitating more efficient immobilization [80].

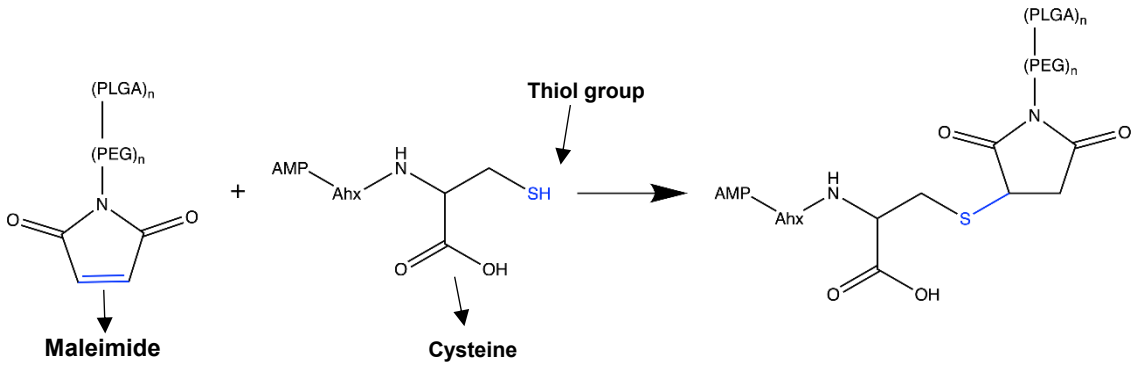


Figure 11- Representation of the thiol-maleimide reaction between PLGA-PEG-Mal and cysteine-modified AMP (AMP-Ahx-Cys). Mal: maleimide group; Ahx: 6-aminohexanoic acid; Cys: cysteine amino acid . Adapted from [81].

2.4.1 PLGA-PEG nanoparticles

PLGA-PEG is a co-polymer constituted by PLGA (poly(D,L-lactide-co-glycolide)) and PEG (polyethylene glycol) (Figure 12). PLGA is a biodegradable polymer, divided into two portions: PLA (poly lactic acid) and PGA (poly glycolic acid) its properties can vary depending on the ratio between these two acids. PLA is hydrophobic and PGA is hydrophilic, which grants amphiphilic properties, important for the formation of NPs [82]. Additionally, PLGA degradation can stimulate tissue regeneration, since, lactic acid is produced in wounds to stimulate collagen production, angiogenesis and, consequently, tissue repair [76].

On the other hand, PEG is a hydrophilic, non-ionic, bioinert polymer and decreases the unspecific adsorption of the therapeutic compounds on NPs surface (opsonization) and increases de exposition of immobilized compounds on the NPs surface [76], [82].

All these characteristics are important for NPs formation, by phenomena like nanoprecipitation [82].

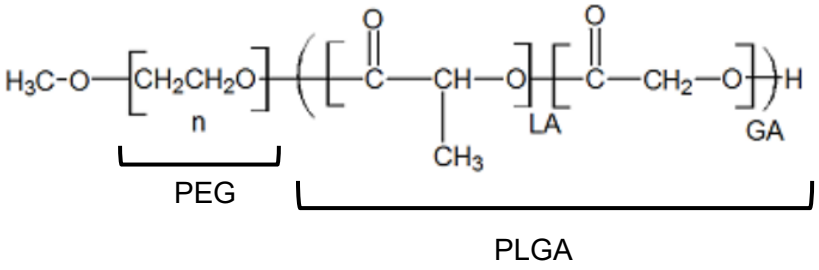


Figure 12- Representation of the chemical structure of PLGA-PEG copolymer. PLGA: poly(D,L-lactide-co-glycolide); PEG: polyethylene glycol; PLA: poly lactic acid monomer; PGA: poly glycolic acid monomer. Adapted from [89]

Aim

The main objective of this master thesis was the development of a smart hydrogel capable of control the release of anti-infected bioactive compounds, namely antisense oligonucleotides (ASOs) and antimicrobial peptides (AMPs) immobilized on nanoparticles, for use as a dressing in the treatment of infected chronic skin wounds. This hydrogel was designed to respond to an endogenous stimulus - ROS produced in infected wounds. The ASOs serve to inhibit gene expression and prevent new biofilm formation after wound debridement, while the AMPs act by killing free bacteria by contact.

The main steps for complete this work are:

1. Development and characterization of MSI78 (AMP)-grafted nanoparticles, as a strategy to prevent rapid proteolytic degradation in vivo, while preserving its antimicrobial activity against *P. aeruginosa*, one of the most problematic bacteria in biofilms.
2. Development and characterization of a ROS-responsive hydrogel:
    - Methylcellulose (MC) was selected because it is degraded by ROS. Its rheological properties were studied to determine which variables (such as MC concentration) can be tuned for future applications as wound dressings. Additionally, the influence of ROS on those properties was evaluated.
    - The capacity of the hydrogel to retain both free compounds (fluorescent ASOs as a model) and immobilized agents (AMP-NP) in the absence of the stimulus was first evaluated. Then, the effect of the ROS on the release kinetics was investigated.

Materials and Methods

1. Nanoparticles (NP) production

1.1 PLGA-PEG NPs

PLGA-PEG NP were produced by nanoprecipitation, according to [76]. For initial release assays, bare NPs (100% PLGA-PEG) were produced by dissolving 20mg of PLGA-PEG (poly(D,L-lactide-co-glycolide) - polyethylene glycol; with 50:50 LA: GA; Mw ≈36000-3000 Da; PolySciTech; Indiana, USA) in acetone (Honeywell, Wabash, Indiana USA) by vortex (VWR VV3). Then, NPs precipitation was made by slowly injecting the NPs in a 10 mL type I water (ultrapure water with a resistivity >18 MΩ cm, a conductivity of <0.056 μS/cm, and <50 ppb of total organic carbons; Merck Millipore) under magnetic stirring (230rpm). These conditions were maintained for 2 hours, for acetone evaporation. In previous washed centrifugal filter units with a 100 kDa nominal molecular weight limit (NMWL) (Amicon, Merck) (type I ultrapure water and ethanol 70%), NPs were centrifuged in a 5810R centrifuge (Eppendorf, Hamburg, Germany) for 10 minutes at 2500 rpm (1188 x g). The concentrated NPs were washed with type I water twice and then collected in a final volume of 1mL.

1.2 Fluorescent PLGA-PEG NPs

Fluorescent NPs were produced using a ratio of 14mg of PLGA-PEG to 6mg of PLGA-PEG-FKR560 (30%) Mw≈3000-36000 Da; PolySciTech; Indiana, USA) dissolved and precipitated in the same conditions as above. These were synthetised aiming to obtain confocal images of the NPs inside the hydrogel.

1.3 PLGA-PEG-Mal NPs and AMP immobilization

Using the same protocol described at 1.1., NPs were produced in a ratio of 12 mg PLGA-PEG to 8mg (40% Mal) PLGA-PEG-Mal (with 50:50 LA:GA) (*Mw* 30000-5000 Da; PolySciTech; Indiana, USA) in sterile conditions.

MSI78-Ahx-Cys (96.9% pure; *Mw* 2694.61 Da; GenScript, Piscataway, New Jersey, USA) was immobilized onto PLGA-PEG-Mal NPs by thiol-maleimide Michael Addition

reaction, as in [76]. 200µL of AMP solution (dissolved in phosphate buffer pH 6.6) were added to 800µL of PLGA-PEG-Mal NP suspension to achieve a 1: 2.5 maleimide-AMP molar ratio. The sample was left overnight in an orbital shaker (110 rpm). On the next day, the sample was transferred to sterilized Amicon filter units and washed 3 times with 10mL of type I water. In the last wash, the samples were centrifuged until residual volumes were below 1mL. Then the volume was made up until 1mL, with type I water and samples were stored at 4ºC until further testing.

1.4 NPs characterization

Size, polydispersity index (PdI) and zeta potential were measured in Zetasizer Nano ZS equipment (Malven Instruments, Malven, UK). The samples were diluted 1:100 in 10mM Sodium Chloride (NaCl) and injected into an electrode-containing folded capillary cell (DTS1070) (Malvern Instruments). The assay was performed at 25ºC after equilibration, with 3 measurements of 12 runs each. The Zeta potential was measured in triplicate too with 10-100 runs with a 15s delay and automatic voltage selection.

NPs quantification was performed through Nanoparticle Tracking Analysis (NTA), in a NanoSight NS300 NTA Dev Build 3.4.4 equiped with a Scmos camera (Malvern Instruments).

1.4.1 AMP quantification

AMP quantification was achieved by fluorometric analysis using the fluorescamine assay according to[76]. Fluorescamine reacts with the primary amino groups of terminal amino acids and lysine, forming a fluorescent pyrrolinone moiety. NPs samples were diluted 1: 4 to guarantee that the fluorescence values were within the range of the respective calibration curve and 150 µL of NPs were mixed with 50 µL of fluorescamine solution at 3 mg/mL. A fluorescamine control with 150 µL of water and 50 µL of fluorescamine solution was also tested. Finally, the fluorescence of the samples was read on a Synergy MX microplate reader (BioTek, Vermont, USA) with 400/460 nm excitation–emission wavelengths. AMP concentrations in the AMP-NP samples were then determined based on the calibration curve by the same procedure. AMP immobilization efficiency (IE%) was determined by dividing the amount of AMP that remains immobilized on the NPs after the last washing step of the preparation protocol by the total added amount.

2. Antimicrobial activity

P. aeruginosa (ATCC 27853) was grown on tryptic soy agar (TSA) plates and Mueller–Hinton Broth (MHB) (Sigma-Aldrich, Missouri, USA).

Minimum inhibitory concentration (MIC) and minimum bactericidal concentration (MBC) were determined through standard broth microdilution assay on microtiter plates, as previously described by [83].

The samples were adjusted according to AMP concentration by dilution in ultrapure water. Controls of bare PLGA-PEG NPs contained the same NP concentration as each AMP-NP sample. 25 µL of diluted sample were added to 75 µL of inoculum adjusted to 2.0 x 10^5 colony forming units (CFU) per mL in MHB on the wells of a round-bottom polypropylene 96-well plate (Corning Incorporated, New York, USA), allowing easy identification of bacterial growth and prevents bacterial adhesion to the walls of the well. To prepare the inoculum, the bacterial suspension was recovered by centrifugation (2700 rpm, 10 min), washed in phosphate buffered saline (PBS), and after a new centrifugation it was resuspended in 5 mL of MHB. The inoculum concentration was adjusted according to the optical density (OD) at 600 nm in MHB. The bacterial inoculum was serially diluted in PBS and plated for CFU counting confirmation. A positive control with 75 µL of inoculum and 25 µL of ultrapure water, a negative control with 75 µL of MHB and 25 µL of ultrapure water, and a negative controls with 25 µL of bNP, AMP-NP and free AMP samples with 75 µL of MHB were also made. The plate was left to incubate at 37 °C for 18–24 h and microbial growth in the bottom of the wells was evaluated by direct observation. The MIC of free MSI78-Ahx-Cys and AMP-NP conjugate was determined as the lowest concentration with an absence of visible growth. The content of the wells without visible growth was then serially diluted to a magnitude of 10^{-7} in PBS and plated for CFU counting. CFUs were counted after an overnight incubation at 37 °C to determine the minimum bactericidal concentration (MBC), the lowest AMP concentration that caused a viability reduction of ≥99.9% of the initial inoculum.

3. ROS production

NIR-LED (25mW/cm^2, 810 nm; Intelligent LED Solutions, UK;) system was coupled to a 6-well plate, in a support, made in-house, design to focus the light on top of each well, perfectly centred, as described in a previous work (Figure 13) [84]. For induction of ROS, MC hydrogels were embedded in 2700 µL of 1X PBS solution (in the 6 well-plate), with the inclusion of 300 µL of Indocyanine green (ICG; Cardiogreen; Sigma Aldrich; St.Louis, Missori. USA) (1mg/mL) and samples were exposed to NIR LED lights for 1h at 37ºC.

3.1 ROS production evaluation

The measurement of ROS production was done by adapting the protocol from Qu *et* al. [55]. Briefly, a solution of 1,3- diphenylisobenzofuran (DPBF; Sigma Aldrich; St.Louis, Missori. USA) was prepared in 25 µg/mL absolute ethanol (AGA; Lisbon, Portugal), in inert conditions. The generation of ROS was evaluated in 2 conditions: a solution of DPBF only or a solution of DPBF-ICG. DPBF solution was injected into the wells (2700 µL per well, in a 6-well plate) plus 300 µL of either distilled water or ICG (1mg/mL). After 1 h of exposure to NIR LED (25 mW/cm^2) at 37 ºC, 3x 100 µL aliquots of the supernatant were transferred to a clear bottom 96-well plate and absorbance at 410 nm was read in a microplate reader (Synergy MX, Biotek).

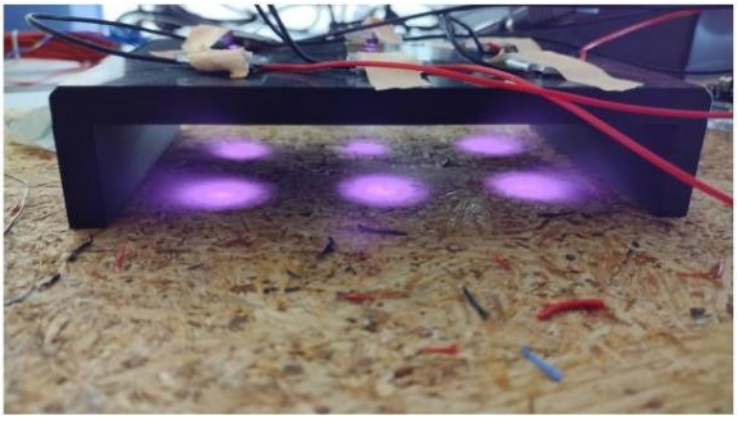


Figure 13- In house NIR-LED system produced by P.Alves [84], fitting 6-well plates, used to produce ROS.

4. Methylcellulose (MC) hydrogels

Methylcellulose (MC; 4000cP; Sigma Aldrich; St.Louis, Missori. USA) solutions were prepared by dispersing the polymer (6%, 7% and 8% w/v) in preheated phosphate buffer saline (PBS) (70ºC) (final concentration in the gel - 1.8X) by vortex at 2500 rpm (1180

Gs) for 3 min (VWR VV3). For formulations containing the bioactive compounds, NPs or free oligonucleotides (sequence in the next section) were added to the PBS solution before mixing with MC (MC-NP or MC-ASOS, respectively). The formulations were stored at 4ºC overnight for complete hydration of the polymer.

For formulations with imbedded fluorescent NPs, laser scanning confocal microscopy (Leica TCS SP5, Leica Microsystems) was performed to obtain images of their distribution in the hydrogel. The objective used was HCX PL APO CS 63x Oil 1.40 NA. The images were taken at 37ºC, using 561 nm laser (51% power) and the emission spectra obtained was set between 575-695 nm, obtaining images from different areas of the hydrogel (pixel size- 240,50 nm). Image processing was performed using Image J software (1.1.0).

4.1 Scanning Electron Microscopy (SEM)

MC hydrogels, subjected or not to ROS through NIR-ICG reaction (4.2.3), were quickly frozen using liquid nitrogen (cryogen). Cryofracturing of the frozen samples was done to obtain images from cross sections of the materials and it was performed using a sharp platinum blade (Astra). Samples were stored at -80ºC. Then, were freeze-dried for 48 h (-88ºC; 323 mT) in a BenchTop PRO with Omnitronics™, from SP Scientific. Lightweight dry hydrogels were mounted onto an aluminium stud and sputter-coated with gold for 30s in a LEICA EM ACE 200. Then, samples cross sections were investigated by a phenom XL scanning electron microscope, in backscattered electron mode (Thermo Scientific) at 5 kV.

4.2 Rheological properties evaluation

The rheological characterization of the hydrogel was performed in a Kinexus Pro, Netzsch. For all the studies, both geometries (upper and lower) were 8mm sandblasted stainless steel parallel plates, using a measuring gap of 500 µm. The formulations were loaded in the lower geometry, then compressed by the equipment, according to the measuring gap and excessive MC was removed. For the determination of the elastic (G') and viscous (G'') moduli, a shear strain sweep protocol was performed ranging from 0.01% to 1000% at 1.6Hz angular frequency. In these assays we, also, studied the influence of ROS in the mechanical properties of the hydrogel. So, before performing the amplitude sweep (shear strain sweep), samples were exposed to NIR LED according to 3.

To determine the gelation temperature, based on [48], a temperature ramp was set, where temperature was increasing 0.5ºC/min from 30ºC to 40ºC at 1% strain. Angular frequencies were recorded at 1,3 and 7 Hz and gelation temperature was determined at the intersection of the resulting tan δ curves.

5. Release assays

5.1 ASOs release and quantification

For oligonucleotide release assays, free fluorescent ASO (Cy3 ASO; Integrated DNA Technologies; Coralville, Iowa, USA: Sequence: 5'end- Cy3 mC* mC* T* mC* T* T* mA* mC* mC* T* mC* mA* mG* T* T* mA*mC*mA; (mN = 2'O methyl RNA; *= phosphorothioate linkage; N = DNA)) was added to the MC in solution (MC-ASOs).

MC-ASOs solutions (40µL) were dispensed into a 24-well plate with one sample per well. The plate was then incubated at 37ºC for 30 min to induce the sol-gel transition.

Then, pre-heated PBS (400 µL, pH 7.4, 37ºC) was added to the wells, to promote ASOs diffusion from MC hydrogels. The samples were then incubated at 37ºC for 72h. At pre-defined time points, the entire supernatant volume was collected for fluorescence quantification and an equal volume of fresh PBS (at 37ºC) was added to each well. At the end of the release assay, all MC-ASOs hydrogels were dissolved in cold type II water (pure water with a resistivity typically between 1 MΩ·cm and 10 MΩ·cm, Merck Millipore), in a cold room (±4ºC) while shaking (150 rpm) and fluorescence was quantified.

Fluorescence was quantified in a Synergy Mx microplate reader (BioTek, Vermont, USA), in a bottom black 96-well plate at 530/580nm emission-excitation wavelength.

5.2 NPs release and quantification

For NP release, 40µL MC-NPs solutions were incubated in a 6-well plate, at 37ºC for 30min, for complete gelation.

5.2.1 ROS-induced release

For induction of ROS, the NIR-LED system was coupled to a 6-well plate. MC hydrogels were embedded in 1X PBS solution, with the inclusion of Indocyanine green (ICG) (1mg/mL) and samples were exposed to NIR LED lights for 1h at 37ºC, as in section 3.1.

5.2.2 Release of Bare-NPs

After NIR-LED exposure of 1h (37ºC), NPs release was evaluated. Aliquots were taken at different time-points (0h, 1h, 24h) while samples stayed in the oven (37ºC) without the NIR-LED. At each time point, the plates were shaken in an Orbital shaker for 5 minutes at 120 rpm, for complete homogenization of NPs, and were diluted (if necessary) to avoid technical issues performing Nanoparticle Tracking Analysis (NTA), performed for NP quantification, in a NanoSight NS300 NTA Dev Build 3.4.4 equipped with a Scmos camera (Malvern Instruments).

6. Statistical analysis

Statistical analysis was performed using GraphPad Prism version 8.0.2 for Windows (GraphPad Software, Califórnia, USA). Data are represented as mean ± standard deviation (SD). Statistical analysis was performed using the t test analysis. Statistical significance was considered when $p < 0.05$ and represented with * for $p < 0.05$, ** for $p < 0.01$, *** for $p < 0.001$, ****$p<0.0001$ and ns (not significant).

Results and discussion

1. Antimicrobial nanoparticles (AMP-NP)

1.1 AMP-NPs characterization

AMP-NPs and bare NP (bNP) were both characterized for the same characteristic (Size and zeta potential). Results obtained using dynamic light scattering (DLS) and electronic light scattering (ELS), are present at Table 1. The average size for AMP-NPs was 182±2nm and for bNP was 109±1nm. The increase in AMP-NP diameter compared to bNP ($p<0.05$ t test) suggests successful AMP grafting. The zeta potential increased from -4.6±0.3mV (bNP) to -0.2±0.2mV (AMP-NP), confirming the presence of the cationic AMP, although the change was not statistically significant. NPs exhibited a polydispersity index (PdI) of 0.23±0.01 for AMP-NPs and 0.12±0.02 for bNPs. The PdI values (<0.3) indicate that both populations are monodispersed. However, to achieve these values for the AMP-NPs, the particles were subjected to a brief sonication process (30 seconds). The need of sonication is supported by PdI values around 0.5 (data not shown) observed immediately after peptide immobilization, indicating NP agglomeration. This

phenomenon may be attributed to the phosphate buffer (pH 6.6) used during NPs production. At this pH, bNPs carry a slightly negative surface charge but AMP immobilization/adsorption leads to a slight increase in surface charge. This shift in zeta potential towards the neutrality may be sufficient to reduce electrostatic repulsion, thereby promoting aggregation.

The amount of MSI78 grafted onto NP surface (IE%) was around 365±35 µg/mL, corresponding to 24% of immobilization efficiency (the results are the average of 3 independent assays with two 2 replicates each from the fluorescamine assay), which is consistent with previously reported values for other MSI78 derivatives [76].

Table 1- Compilation of the characterization of every PLGA-PEG NP formulation through DLS and ELS (these are the results from 3 independent assays, with 3 replicates each): AMP-NP (AMP grafted onto PLGA-PEG-Mal-NP). bNP (bare PLGA-PEG-NP). Fluorescent bNP (FKR560 bare PLGA-PEG-NP); Both AMP-NPs and Fluorescent bNP are exclusively compared (statistically) with bNP using t test; Statistically significant differences are indicated as *p < 0.05 and ns (not significant).

PLGA-PEG NPs	Average size (nm)	Polidispersity Index (PdI)	Zeta Potential (mV)
AMP- NP	182±2 (*)	0.23±0.01 (*)	-0.2±0.2 (ns)
Bare NP (bNP)	109±1	0.12±0.02	-4.6±0.3
Fluorescent bNP	129±1 (*)	0.08±0.01 (ns)	-1.7±0.6 (ns)

Concerning fluorescent NP (table 1), there is an increase in size relative to bNPs (129±1 nm), which is due the presence of the fluorophore (FKR560). The PdI did not change significantly, and the Zeta potential increased to -1.7±0.6. This increase in surface charge did not aggregate the NPs, as we can see for the PdI values very close to 0. This could be justified by the fact that FKR560 is neutral and its addiction to PLGA-PEG may cover some potential negative groups, like carboxyl groups from PLGA, increasing the surface charge.

NP were also quantified by nanoparticle tracking analysis (NTA) showing a concentration of $1.7x10^{12} \pm 9.3x10^{11}$ NP/mL for each production batch (PLGA-PEG NPs were used for this quantification and the results were assumed to be the same for the other batches, fluorescent NPs and AMP-NPs; one independent assay with two replicates).

2. AMP-NP antimicrobial activity

The antimicrobial activity of AMP-NP and free MSI78-Ahx-Cys (AMP) was evaluated against *P. aeruginosa*. The initial inoculum (average value of 2 independent assays - $1x10^6$ CFU/mL) was incubated in successive concentrations of AMP (0.250-128 µg/mL), for free AMP and AMP-NP, overnight. In a first analyse, no antimicrobial activity was seen for the bNPs, which emphasizes that PLGA-PEG does not possess antimicrobial potential. Secondly, both AMP and AMP-NP showed significant antimicrobial activity. The MIC obtained for free AMP was 8-16 µg/mL and the MBC for the same condition was 8-32 µg/mL (Table 2). There is an increase of these values against *P.aeruginosa* (ATCC 27853), comparing to the previous work for MSI78 without the spacer (Ahx) and the extra cysteine amino acid (Cys) with MIC values of 0.5-1 µg/mL and MBC was 1-4 µg/mL [85]. These differences could be explained not only by the variations in AMP composition, but also in divergencies in the experimental protocols, namely the use of TSA in this study instead of TSB for initial bacteria growth, the use of water rather than BSA solution to dissolve AMP and AMP-NP, and the lower AMP-to-bacteria ratio (1:10 instead of 1:4) [85]

The MIC obtained for AMP-NP was 64 µg/mL and the MBC was 128µg/mL or higher (Table 2). A notable decrease in antimicrobial activity was observed when comparing free AMP to AMP-NP, indicating that the grafting process reduced the AMP activity (both bacteriostatic and bactericidal – was reduced by approximately 4x). A 99% reduction in bacterial viability was achieved only at concentrations of 128µg/mL or higher. Although this reduction does not reach 99.9%, it is important to note that at 128 µg/mL, that bacterial regrowth was only observed in 1 replicate with a final concentration of 4×10^4 CFU/mL after overnight incubation. This residual growth suggests that the MBC concentration of AMP-NP may exceed 128 µg/mL. Nevertheless, this MBC value was determined based on a single independent experiment (three replicates) and should be confirmed by repetition with additional replicates and higher AMP-NP concentrations.

This attenuation of overall antimicrobial activity may be explained by the weaker interaction of the grafted peptide with the outer membrane components, once the overall charge of the NPs is very close to 0 mV, which may influence the attraction. Also, when immobilized in NPs, AMPs and NP components can be so tightly bonded and packed that they lose mobility and may be less exposed to the external environment, as covering up the hydrophobic portion of the peptide, which may decrease the penetration capacity in the membranes and, consequently, the activity of the AMP.

Table 2- Antimicrobial activity of AMP (MSI78-Ahx-Cys) and AMP-NP (MSI78-grafted onto PLGA-PEG-Mal-NPs). Minimal Inhibitory concentration (MIC) and Minimal bactericidal concentration (MBC) values expressed in µg/mL. These values are a result of 2 independent experiments with 3 replicates for free AMP and 1 experiment with 3 replicates for AMP-NP.

	P.aeruginosa (ATCC 27853)	
	MIC(µg/mL)	MBC(µg/mL)
AMP	8-16	8-32
AMP-NP	64	≥128

3. ROS production evaluation

To confirm the generation of ROS in the presence of Indocyanine green (ICG) upon irradiation by the near-infrared (NIR) light (the setup described in the methodology, section 3.), a ROS-sensitive compound, 1,3- diphenylisobenzofuran (DPBF) was used. The concentration of DPBF can be followed by UV-Vis absorption at 410 nm. In the presence of $^1O_2$ (ROS generated by ICG under NIR irradiation)[84], DPBF is converted to 1,2-dibenzoylbenzene, a compound that does not absorb at 410 nm [55]. Therefore, a decrease in DPBF concentration is expected when ICG generates ROS upon NIR light exposure.

The results obtained from this study are shown in Figure 14. When ICG was irradiated by NIR light (NIR ON), a drastic decrease in DPBF concentration (final concentration was 32%) was observed, indicating successful generation of ROS. This decrease is attributed to the conversion of DPBF into a compound that does not absorb at 410 nm. In contrast, only a minimal decrease of DPBF was observed in the absence of ICG (NIR ON) and when NIR irradiation was absent (NIR OFF) (final concentrations were 99% and 97% respectively), validating the combined use of the NIR-LED system and ICG for ROS generation.

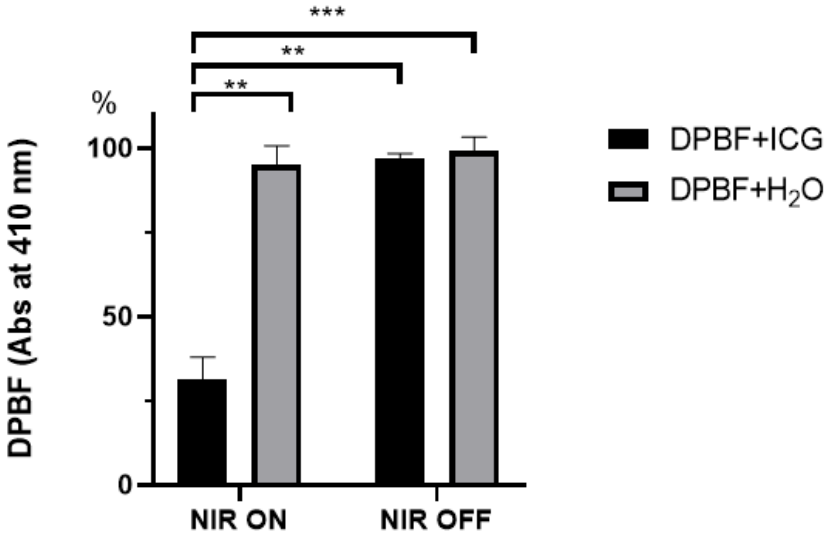


Figure 14- Quantification of ROS-triggered conversion of DPBF to a compound non-detectable at 410nm, in two tested conditions when NIR was ON and OFF. These are the results of two independent assays with 3 replicates each. Statistically significant differences are indicated as *p < 0.05; **p < 0.01; ***p < 0.001 and ns (not significant).

4. Methylcellulose (MC) hydrogel

After overnight storage at 4ºC, complete hydration of the polymer (MC) was observed, resulting in a transparent solution, as shown in Figure 15 (left). Although these solutions were highly viscous and difficult to pipet, due to the high viscosity grade of the MC used (4000cP), the hydrogel formation only occurred after thermal transition. Gelation was achieved after 30 min incubation at 37ºC, resulting in a formation of a strong and turbid hydrogel (Figure 15, right). This step, which ensures consistent gelation of all samples, is based on previous studies conducted by our group and is sufficient to induce the phase transition from liquid-like solution to a hydrogel.



Figure 15- Gel transition from a transparent solution (left) and the formation of the hydrogel (right), which turns turbid and keeps the format of the Eppendorf tube if pulled out.

4.1 Rheological properties evaluation

4.1.1 Gelation temperature determination

Gelation temperature (T_G) is the point at which the solutions transit to a stiff hydrogel. One common way to determine T_G is by analysing the interception between G'' and G', during a temperature ramp. Initially, G'' is higher than G' reflecting the liquid-like behaviour of the sample. As the temperature increases, a transition occurs T_G, where G' surpasses G'' indicating the formation of a more solid-like hydrogel network.

Figure 16 shows how G' and G'' change in 8% MC solutions during temperature increase. Between 30 ºC and 40 ºC, G' is always higher than G''. The fact that G' is higher than G'' at all frequencies aligns with the observation that MC solutions are hard to pipette and already behave like a solid, even though no clear phase transition has occurred yet. Additionally, as the temperature rises above 34 ºC, the G' values from the 3 tested angular frequencies (1, 3 and 7Hz) start to converge. However, according to [86], the material is still considered in solution, since G' remains dependent of the

frequency. The convergence of G' values of the 3 frequencies at higher temperatures may suggest a loss of frequency dependence, possibly indicating the beginning of gelation. Still, the phase transition is not very clear in this analysis, not allowing T_G determination based on the viscoelastic moduli (G' and G'').

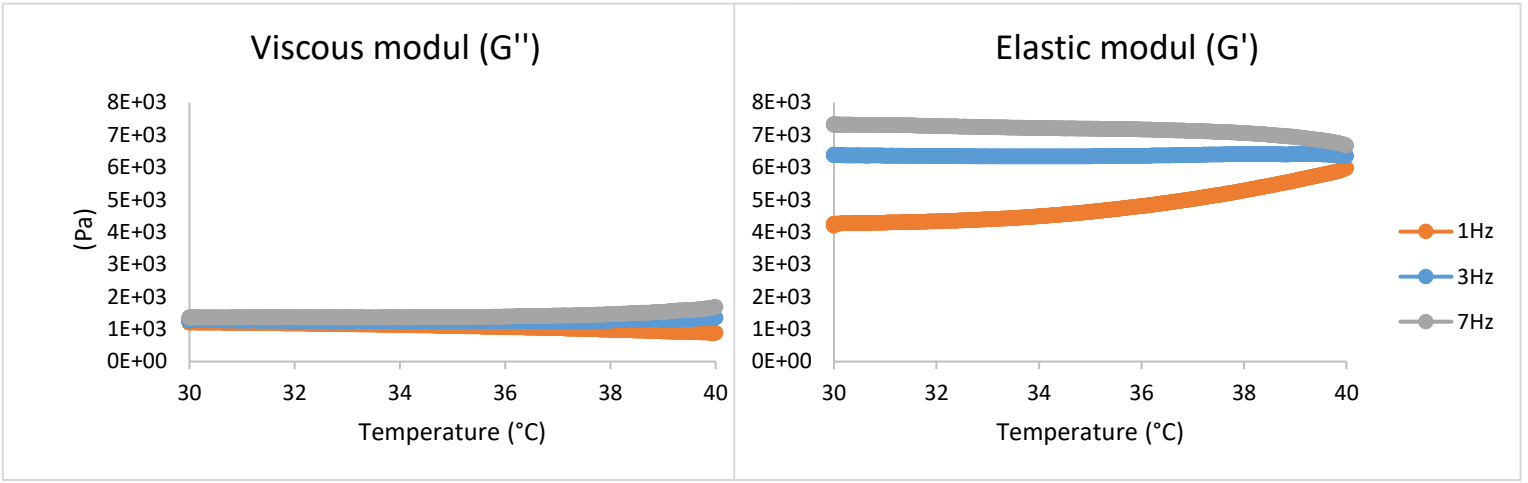


Figure 16- Variation of G'' and G' of 8% MC solutions upon heating, according to different angular frequencies. On the left it is possible to see the variation of temperature on G''. On the left it is possible to see the influence of temperature in G', showing frequency dependence at lower temperature and losing that dependency at higher temperatures. This is a result of 1 independent assay.

Another way to observe this phase transition is by analysing the tan δ. As described in [48], tan δ (the ration of G'' to G'), can be used to determine T_G of hydrogels. Also known as the loss tangent, it shows how much energy is lost compared with how much is stored in the material, helping to identify the point where the solution becomes a hydrogel. [44]

Figure 17 shows the tan δ variation graph, in which all tested angular frequencies tend to converge at a specific point. According to the protocol described in [48], the key indicator of gelation is the interception of these curves. In this case, the curves intercept and overlap between 37 ºC and 37.5 ºC, which can be considered the gelation temperature for this formulation.

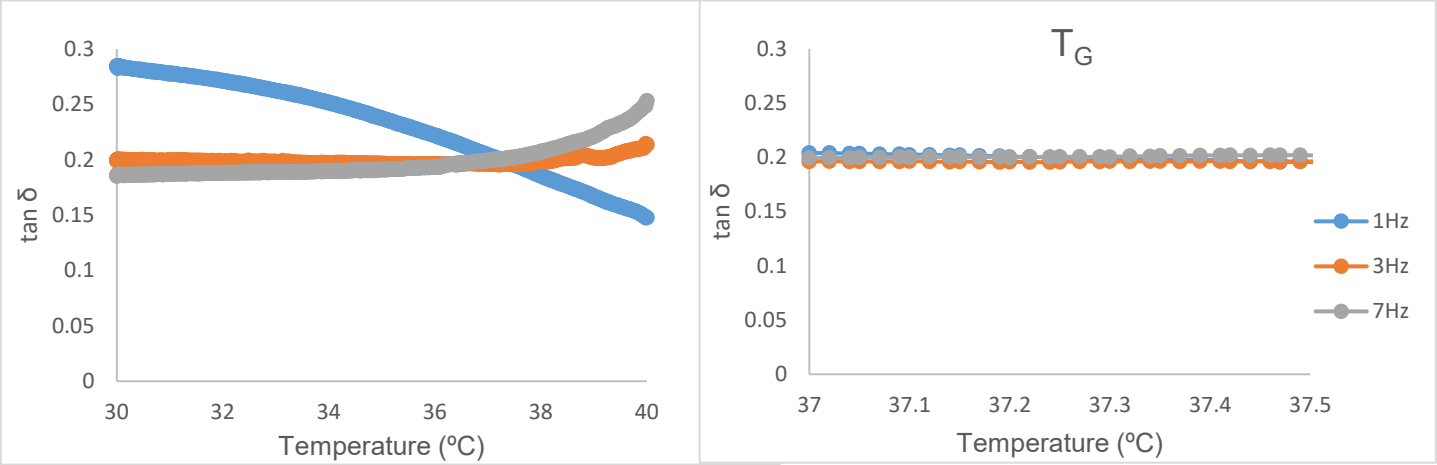


Figure 17- Variation of tan δ of 8% MC solutions upon heating, according to different angular frequencies. The left graphic shows the entire data for 3 angular frequencies tested (1, 3 and 7 Hz), where is possible to see the intersection point. On the right graphic it is possible to see the intersection of the curves between 37 and 37.5ºC. This is a result of 1 independent assay.

4.1.2 MC hydrogel mechanical properties

The shear stress sweep assay, which determines the material resistance to increasing deformation, was performed to evaluate the hydrogel stiffness and mechanical resistance by determining the limits of the linear viscoelastic region (LVER), studied through storage modulus (G') and loss modulus (G'') evaluation.

The mechanical properties of hydrogels prepared using 6% and 8% MC was compared (Figure 18). For both conditions, the graphs show the LVER region, where the values of G' and G'' remains stable (graphs 1 and 2) and, when the deformation (Y*%) reaches a critical value, the moduli cross, indicating the point where hydrogel collapses (graphs 3 and 4). Comparing graphs 1 and 2, it is evident that LVER does not change significantly between conditions (6% and 8% MC) as the values of both moduli are very similar. However, the slightly higher G' values in the 8% MC hydrogel ($5.5x10^3 \pm 1.9x10^3$ Pa versus $2.2x10^3 \pm 3.67x10^2$ Pa for 6% MC) are consistent with expectations, since higher polymer concentrations typically result in increased stiffness. On the other hand, analysing the final portion of the overall graphs (3 and 4) the interception of the curves occurs at a higher shear strain in the 6% MC hydrogel (126% versus 50% at 8% MC). This indicates that, although the elastic module (G') is lower than that on the 8% MC sample, the 6% MC hydrogel resists better to deformation. In contrast, the 8% MC hydrogel exhibits more brittle behaviour breaking at lower shear strain values (p <0.0001).

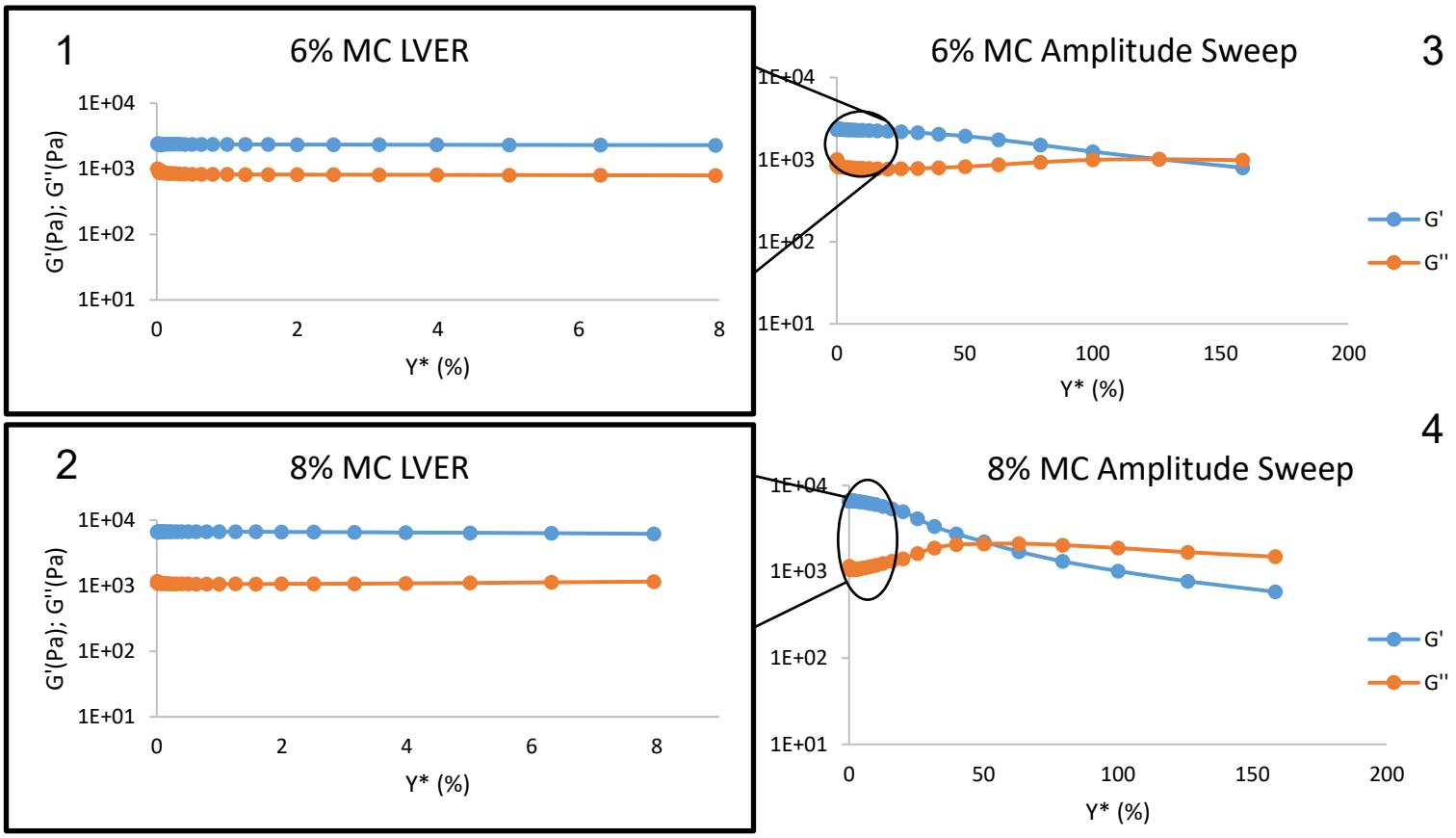


Figure 18- Resulting graphics from the amplitude sweep assay. Graphs 1 and 3 represent the mechanical properties of 6% (w/v) MC hydrogel, while graphs 2 and 4 correspond to the 8% (w/v) MC hydrogel. Graphs 3 and 4 display the full-scale data for both hydrogels. The dark circles on graphs 3 and 4 highlight the LVER region, which is zoomed in on graphs 1 and 2 on the left. Results for both conditions are based on 3 independent assays. Statistically significant differences are indicated as *p < 0.05; **p < 0.01; ***p < 0.001, ****p< 0.0001 and ns (not significant) determined by t-test.

4.1.3 ROS influence in MC hydrogels mechanical properties

This study aims to determine the influence of ROS on the mechanical properties of MC hydrogels as an indicator of their degradation, and consequently, their potential as ROS-responsive drug delivery system. Hydrogels prepared using two different MC concentrations (6% and 8%) were compared after exposure to ROS generated by ICG under NIR-LED irradiation (1h), as described in section 3 of materials and methods. Results from the amplitude sweep assays are presented in Figure 19.

Analysing a portion of the LVER, we observe that for both concentrations, the loss module (G'') was lower in the presence of ROS (NIR are ON) compared to when NIR is OFF (6% MC: NIR ON = 234 ± 16 Pa; NIR OFF= 324 ± 14 Pa; 8% MC: NIR ON= 335 ± 45 Pa; NIR OFF=769 ± 277 Pa). On the other hand, no significant changes were observed in the elastic module (G'). The decrease in the hydrogel's loss module upon exposure to ROS (NIR ON) aligns with findings reported by [54], which indicates that singlet oxygen ($^1O_2$) generated by ICG irradiation under NIR LED light can reduce viscosity of MC by up to 50% suggesting chain degradation.

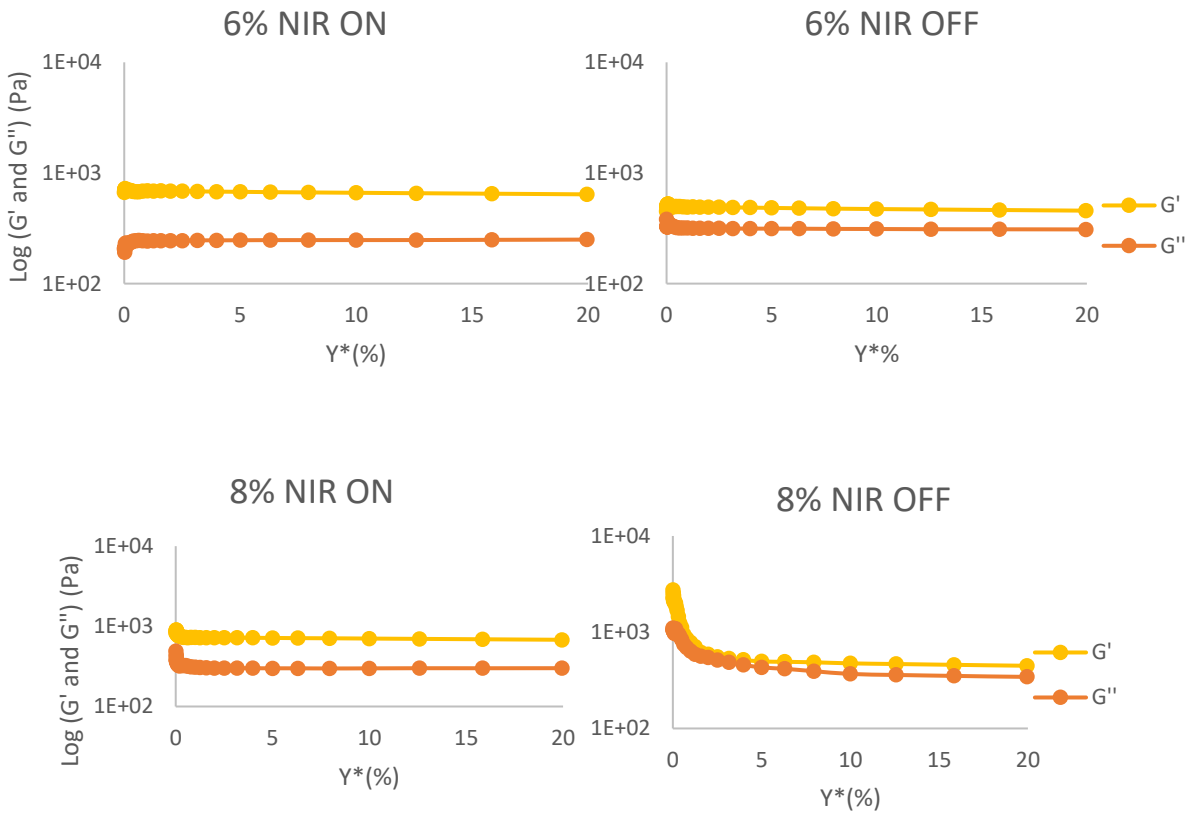


Figure 19- Resulting graphics from the amplitude sweep assay showing the influence of ROS in G' and G'' of MC hydrogels (6% and 8%) within the LVER region. These graphs represent data from one independent assay. Statistically significant differences are indicated as *p < 0.05; **p < 0.01; ***p < 0.001, ****p< 0.0001 and ns (not significant). Comparisons were made only between NIR ON and NIR OFF for each concentration using the t-test.

We may be observing a material modification, as there is a highly significant change in G'' ($p<0.0001$), in the presence of ROS. However, a decrease of G' would also be expected, indicating a reduction in molecular weight and a loosening of the mesh structure due to the cleavage of glycosidic bonds.

4.2 MC hydrogels morphology

The morphology of hydrogels produced using different MC concentrations (6 and 8%) was evaluated by scanning electron microscopy (SEM). SEM images of hydrogel cross-sections are showing at Figure 20. Analysing the cross-section images obtained from backscatter electrons, it is possible to see highly porous hydrogels, presenting micrometric pores and numerous compact layers of MC fibres.

By comparing the images of the hydrogels prepared with 8% MC with 6% MC (Figure 20), clear differences in pores shape and fibres thickness are evident. However, these differences can be explained by the fact that images of the 8% MC hydrogel were obtained from a surface section, whereas the images of 6% MC hydrogel were taken from a cross-section cut with a blade. For this reason, comparing pores shape is a challenge, as pore formation on the surface may result from depolymerization of the hydrogel occurring between samples removing from the oven and freezing with nitrogen. Additionally, surface pores may be originated from bubbles formed when the MC solutions are extruded onto the plate and from sample manipulation during mounting on the SEM studs. Additional SEM studies should be performed to complement these assays.

Still, the observed micrometric porous suggest that small compounds (with angstrom and nanometric-scale sizes) may be passively released through this mesh. However, for larger compounds, the multiple layers composing the hydrogel are expected to create significant physical resistance, reducing the passive release of compounds.

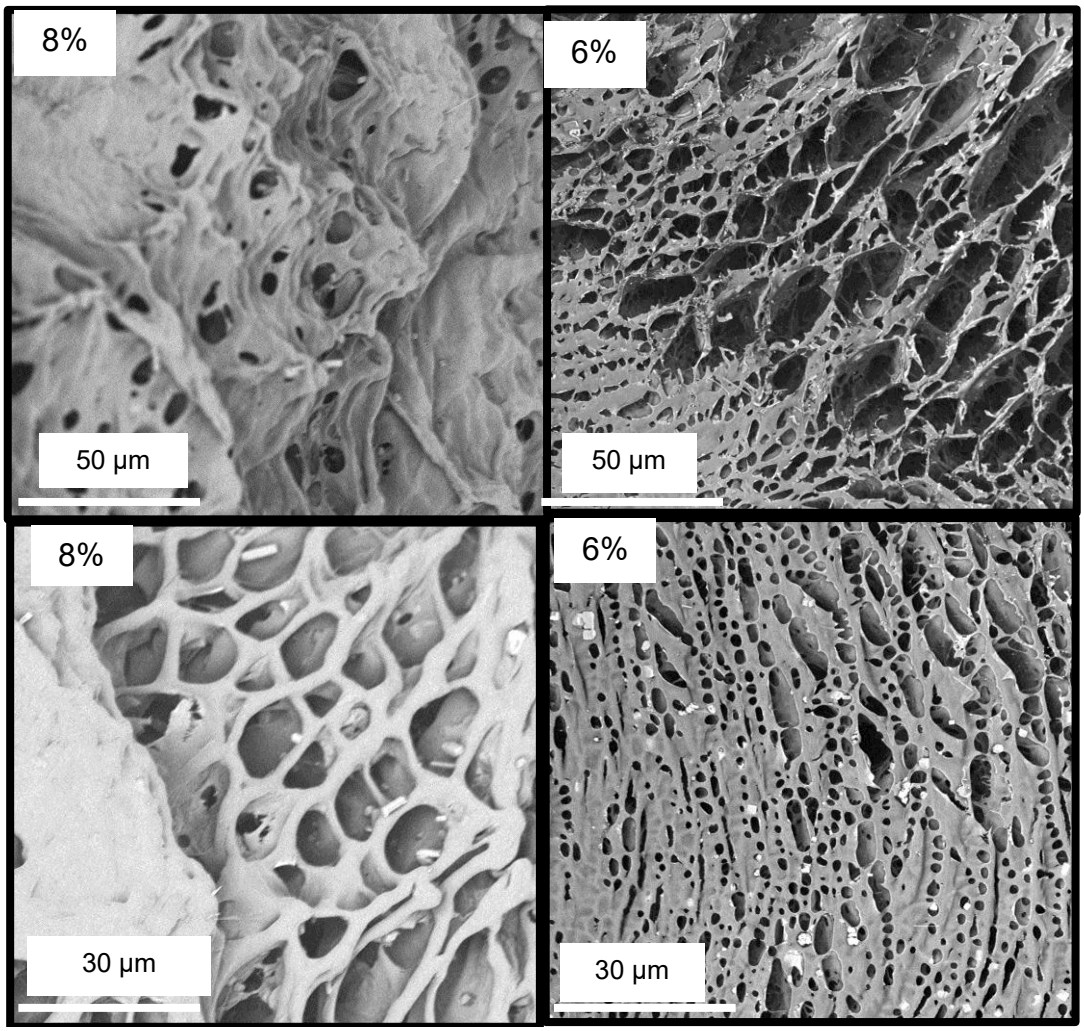


Figure 20- SEM images comparing 8% MC hydrogel (two images on the left) with 6%MC hydrogel (two images on the right. For both conditions the scales are represented on the bottom. Only 50 µm and 30 µm scales were compared for all the images taken. Images from 8% MC were taken of a portion of the surface of the hydrogel, instead of cross-section, due to difficulties on identifying the cross-section site of the samples after freeze-dried.

The influence of ROS in the morphology of the 8% MC hydrogel after NIR irradiation in the presence of ICG was also evaluated by SEM (Figure 21). ROS generation (8%NIR ON) may have caused changes in the fibres, as very fine and seemly fragile fibres can be observed inside the pores particularly near the cross-section plane. This effect was not seen when the NIR irradiation was OFF, where no sighs of degradation are visible and thick fibres forming the pores are observed. However, the direct comparison with the hydrogel without ROS is difficult because images of cross-sections without ROS are not available (only surface images exist).

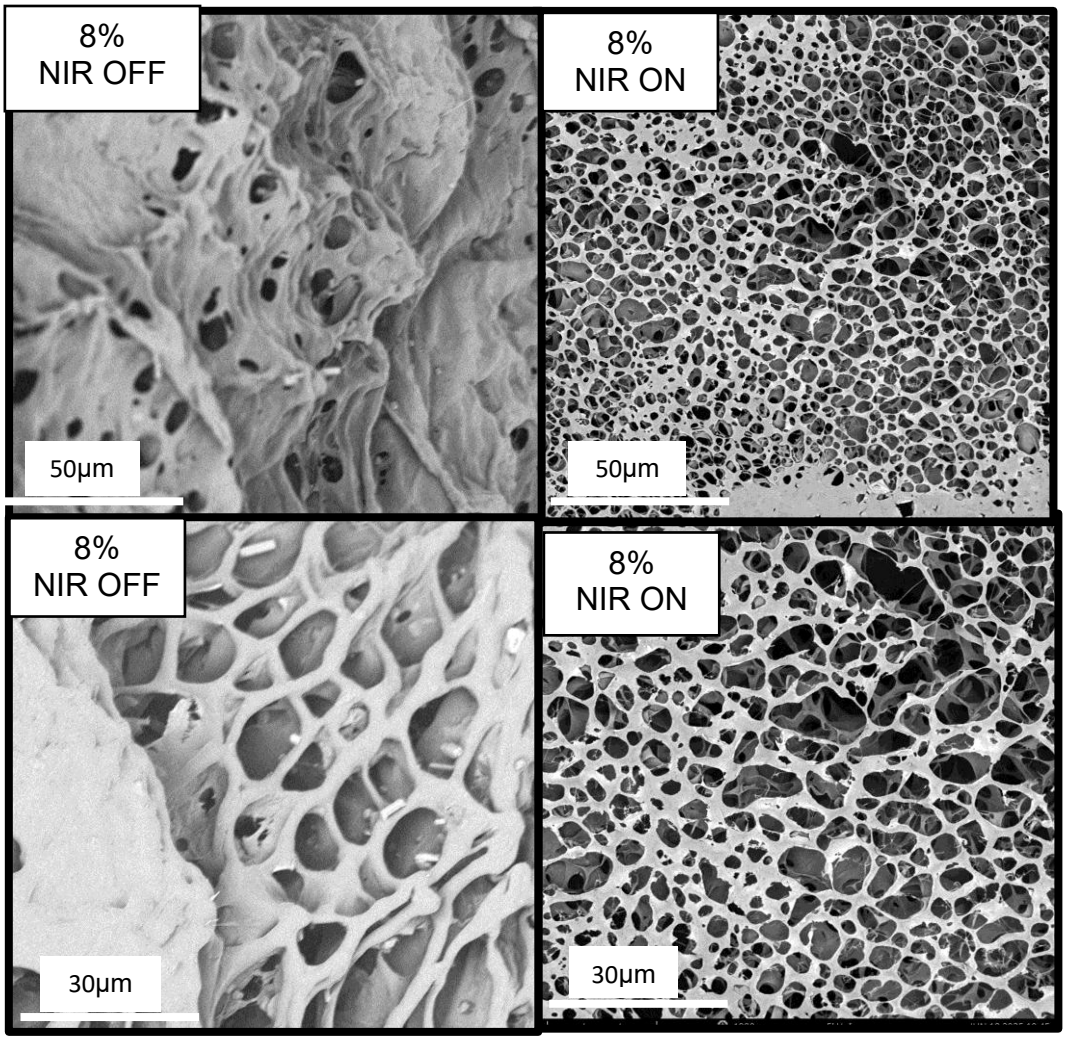


Figure 21- SEM images comparing 8%MC hydrogels when the NIR are OFF (two images on the left) with when the NIR are ON (two images on the right. In the 8% NIR ON image (30 µm) it is possible to see fine fibres from deeper layers, as described in the text, which is not seen in the 8% NIR OFF corresponding image. For both conditions the scales are represented on the bottom. Only 50 µm and 30 µm scales were compared for all the images taken. Images from 8% NIR ON were taken of a portion of the surface of the hydrogel, instead of cross-section, due to difficulties on identifying the cross-section site of the samples after freeze-dried.

5. Release assay

5.1 ASOs release from MC hydrogels

The objective of this study was to select the MC concentration required to prepare a hydrogel capable of retaining ASOs in the absence of ROS, for used in the development of a smart delivery system that responds specifically to a ROS stimulus. The release studies kinetics, assessed by the incorporation of a model fluorescent ASOs (Cy3 ASO) into MC hydrogels (MC-ASOs), are presented in Figure 22. ASO release was monitored

over 72 h using three different MC-ASOs formulations prepared using different MC concentrations (6, 7 and 8%). MC hydrogels prepared with the same MC concentrations but without Cy3 ASO were used as controls for comparison.

The results show an exponential release of Cy3 ASO within the first 24h for all samples followed by a plateau in the release profile (Figure 22). This plateau reflects the complete release of ASOs (near 100% release) after 1 day of experiment. After 72h, no significant fluorescent signal was detected, indicating that all the Cy3-ASO had already been released. To prove that all the ASOs were released, at the end of the assay, the hydrogel was dissolved, and the fluorescence of the resulting solution was quantified. No fluorescence was detected in any sample indicating the absence of ASOs inside the MC hydrogels independently of the MC concentration used in the preparation. Also, the control samples do not exhibit fluorescence, which means that PBS and MC do not interfere with the results.

These results demonstrate that MC hydrogels are unable to retain free ASOs within its mesh, regardless of MC concentration. This is likely due to the considerable size difference between the small oligonucleotide molecules and the relatively large pores of the hydrogels. Given the helical structure and the angstrom-scale width of ASOs, they are likely to small to be physically retained and thus diffuse rapidly out of the hydrogel matrix. One potential solution to this limitation could be increasing the size of the antimicrobial agent by ASOs immobilization onto NPs surface [59].

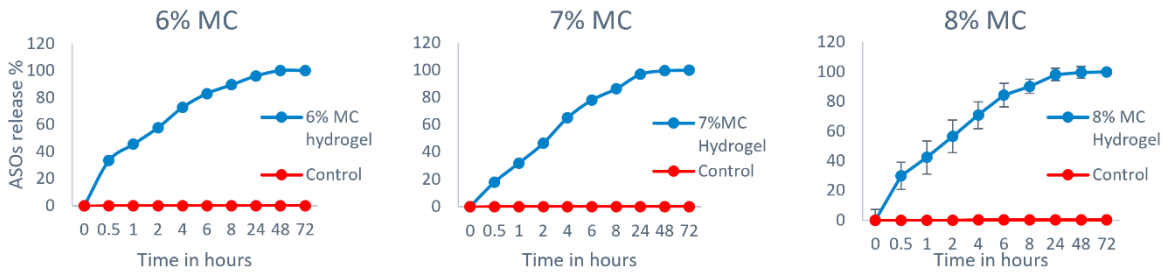


Figure 22- ASOs release profile in different MC hydrogels (6,7 and 8% w/v). Every sample was compared to MC hydrogel without ASOs. For each concentration, the results shown are the result of 3 independent assays. Deviation between replicates is represented in all the graphics, although cannot be clearly seen in 6 and 7%, since it is so low.

5.2 NP release from MC hydrogels

5.2.1 NP distribution into the MC hydrogel

Fluorescent NP-MC hydrogels were produced to visualize the distribution of fluorescent PLGA-PEG NPs inside the MC hydrogel mesh (Figure 23) Confocal microscopy images were acquired from different regions of the hydrogel. To confirm that MC does not interfere with fluorescence signal quantification due to autofluorescence, control images of hydrogels without NP (MC only) were acquired. No detectable fluorescence at the excitation/emission wavelengths used was observed.

The images show a homogenous distribution of fluorescent PLGA-PEG NPs through the hydrogel mesh. Some localized regions of higher fluorescence intensity were observed, which may correspond to NP agglomeration.

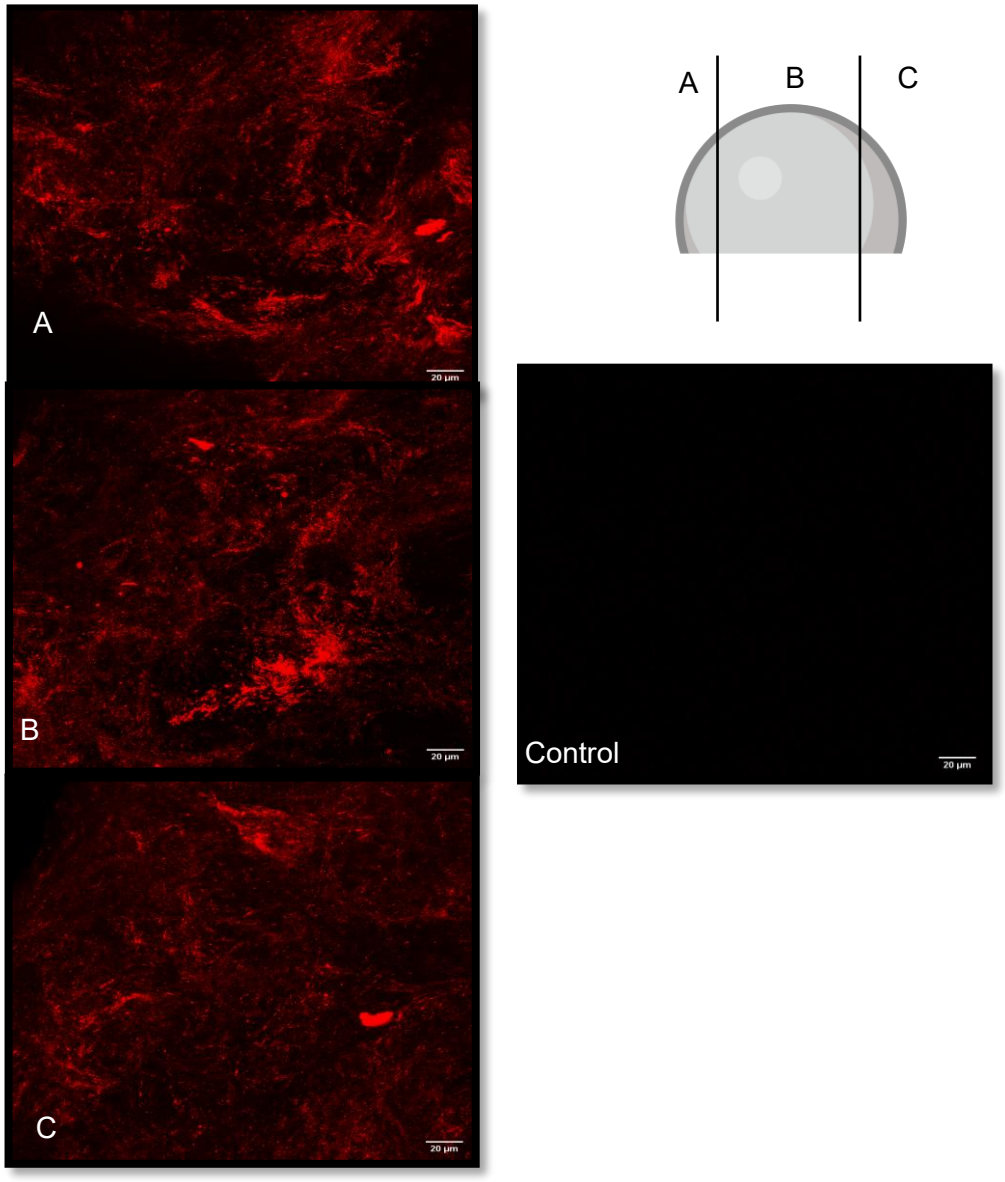


Figure 23- NP distribution profile in 8% MC hydrogel visualized by confocal microscopy. A schematic diagram at the top right of the figure view that indicates the hydrogel regions corresponding to each confocal image (A, B, and C). Red signals represent the fluorophore incorporated in PLGA-PEG-FKR560 NPs (30%). The isolated image at right shows the control hydrogel (without fluorescent PLGA-PEG NPs).

5.2.2 Effect of ROS on NP release from MC hydrogels

The aim of this assay is to evaluate whether bare NP (bNP) embedded into hydrogels prepared with 6% and 8% MC can be effectively released in the presence of ROS generated by ICG upon irradiation with a NIR-LED light (1h). The results from the release assay are shown in Figure 24. All the hydrogels started with an initial NP concentration $3.2x10^{12}$ NP/mL. The graphs show higher NP release for hydrogels prepared with 6% MC (ns; p=1.6 for NIR ON and OFF). The difference in NP release between presence (NIR ON) and absence (NIR OFF) of ROS was 37%. Although this difference was not

statistically significant (p=0.15), it still indicates a notable effect of the ROS stimulus. For 6% MC, the difference was smaller and less significant (14%; p =0.75). Still, NP release was enhanced at both concentrations under NIR irradiation. These differences may be explained by the fact that higher polymer concentrations increase the number of MC fibres layers, making NP diffusion more difficult in the absence of ROS stimulus. In contrast, lower MC concentrations form fewer fibres and layers, allowing NPs to pass through the mesh more easily without any stimulus. Additionally, release was enhanced at both concentrations under NIR irradiation, suggesting some MC hydrogel degradation.

It was also shown that, although the release was high in all the conditions for both MC concentrations (over $1x10^9$ NP/mL), only around 0.14% (average value for all the conditions – both concentrations, NIR ON and OFF) was released after 24h. This confirms that using larger size nanoparticles (regarding to molecules) helped in reducing the release rate.

.

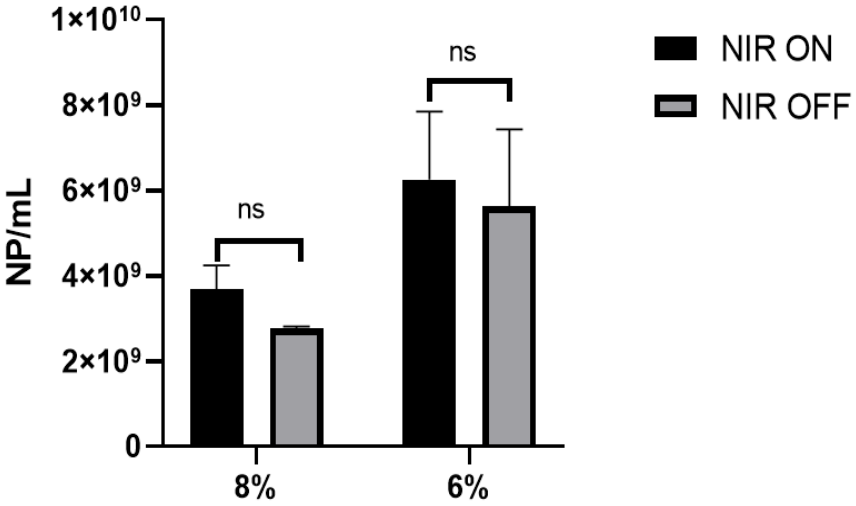


Figure 24- NPs release from the hydrogel after 24h. The results shown are the cumulative of timepoint 0h,1h and 24h, originated by 2 independent experiments: The total amount of NPs released for both concentrations is very low in comparison to the initial concentration of NPs included in the hydrogel (3.2e12 NP/mL); It is possible to see clear differences between samples with and without ROS (NIR ON vs NIR OFF), specially at 8% MC. Statistically significant differences are indicated as *p < 0.05; **p < 0.01; ***p < 0.001 and ns (not significant).

6. General conclusions and future work

The aim of this work was the development of antimicrobial hydrogels for the treatment and prevention of infected skin wounds. Since reactive oxygen species (ROS) levels typically elevated in infected wounds, methylcellulose (MC) hydrogels, which are sensitive to ROS, can be used as infection-responsive controlled released system triggered by this endogen stimulus. MC hydrogels can be produced using a simple and highly reproducible method. Different MC hydrogels can be easily produced using varying MC concentrations, with ability to incorporate diverse compounds, including anti-infected molecules and nanoparticles (NP), for controlled delivery.

Several conclusions were obtained from this thesis:

MC hydrogels were formed using both 6% and 8% MC concentrations after 30 min at 37ºC. SEM images showed that both hydrogels had a high pore density at the micrometre scale. However, differences between 6% and 8% were inconclusive. Further morphology studies should be repeated in order to investigate if there are differences in pore size and fibres thickness, between concentrations.

Rheological properties of MC hydrogels changed significantly with polymer concentrations, becoming more brittle at high concentrations of the polymer (8%MC), and more resistant against shear strain, when concentration is lower (6% MC). Also, T_G determination assay suggested that phase transition can happen around 37ºC, although these tests must be repeated for 8% MC. Additionally, it would be important to investigate the T_G of 6% MC to conclude how concentration interferes with this parameter.

Release assays demonstrated that the MC hydrogel can only retain high molecular weight compounds. This indicates that, neither free antisense oligonucleotides (ASOs) nor free antimicrobial peptides (AMPs), are suitable for this smart delivery system, as their molecular sizes are too small to be effectively retained for a controlled released. In this work, the release of free AMPs was not evaluated, as it was assumed that the outcome would be similar to that observed with ASOs, which easily diffused through the hydrogel mesh in the absence of ROS. A potential solution could be to immobilize the ASOs on NPs surface[59]. Nevertheless, the activity of grafted ASOs must be tested. If grafting compromise their activity, ASOs should be loaded onto the NP to enable their released at the wound site.

Monodispersed Bare PLGA-PEG-NPs (bNP) with an average size of 109 ± 1 nm and -4.6 ± 0.3 mV charge, were successfully produced and incorporated into MC hydrogels in

a concentration of $1.7x10^{12} \pm 9.3x10^{11}$ NP/mL. Their uniform distribution within the MC hydrogel was demonstrated using fluorescently labelled NPs (using PLGA-PEG-FKR560) observed by confocal microscopy.

The release of bNPs was not entirely controlled by ROS, but it was accelerated in the presence of ROS, particularly in 8% MC hydrogels. This suggests that the NPs are still small enough, relatively to the hydrogel pore size, to passively diffuse through. The response to ROS was more pronounced in 8% MC hydrogels, probably because the denser network of MC fibres creates more barriers compared to the 6% MC, resulting in a higher release when stimulated. Nevertheless, the effect of ROS on the morphology of the hydrogels with 8% MC (SEM) suggested some degradation when ROS were generated, forming fine and fragile fibres. Both the release of bNPs and SEM studies should be repeated in the future to (i) clearly prove that the release of NPs is accelerated by ROS and (ii) confirm that this increased release is caused by MC degradation induced by ROS. Other imaging techniques could also be explored. Transmission electron microscopy (TEM), using a technic which consists of embed the samples in liquid resin, so it fills the pores of the hydrogel, and, after solidification and the cutting of thin slices, it is possible to take images from difference layers. This technique undergoes the problem of losing the cross section of the sample, which happened in this work. Not discarding completely SEM, there are more advanced models of this equipment that allow the rotation of the sample, during the analysis, such as FEG-SEM, which, not only offers better resolutions, but also allows the manipulation of the sample during the analysis.

The influence of ROS on the rheological properties was suggested, according to [54], as a significant decrease in G'' was observed on both hydrogels tested (6% and 8% MC) when ROS were generated. However, additional replicates of this assay are necessary to reach more definitive conclusions.

The AMP (MSI78-AhX-Cys) demonstrated to be bactericidal to *P. aeruginosa* at concentrations of 8-32 µg/mL. This AMP was successfully grafted onto PLGA-PEG-Mal NPs (182±2 nm and -0.2±0.2 mV) with an immobilization yield of 24 % (365±35 µg/mL).

The antimicrobial activity of AMP-NPs was four times lower compared to the free AMP, consistent with previous studies using other AMP [76]. This reduction may be related to the fact that the AMP mechanism of action is different when immobilized [67]. The mechanism of action of MSI78 (similar with MSI78-AhX-Cys) involves disrupting bacterial membranes by forming toroidal-type pores [68]. When grafted onto NP, the immobilized AMPs induce destabilization of the membrane potential and activation of bacteria

autolytic enzymes. These enzymes trigger a cascade of intracellular degradation events, leading to increase water influx and elevated internal cells pressure, causing bacteria cell death. These changes in the AMP mechanism of action, due to reduced AMP mobility and decreased exposure to bacterial targets, may contribute to the observed decrease in antimicrobial activity. More replicates of this assays must be done too. Additionally, as future work, it would be interesting to investigate the influence of ASOs on biofilm formation and how their immobilization influences the knockout of related genes.

Still, the MSI78-AhX-Cys concentrations needed for bacteriostatic and bactericidal effects (MIC and MBC) remain relatively low, which is very positive given that similar MSI78 in solution has been reported to exhibit haemolytic activity at high doses (128 µg/mL causing 13% haemolysis) [85]. Additionally, for future work, it would be interesting to test the cytotoxicity of MSI78-AhX-Cys, especially after grafting onto NP (AMP-NPs), at concentrations ≥128 µg/mL. Since the antimicrobial activity decreases upon immobilization, it is possible that cytotoxicity may also be reduced. Moreover, it is also important to test the antimicrobial activity of both free AMP and AMP-NPs in simulated wound fluid (SWF). This will help to understand if immobilization protects the AMP from proteolytic enzymes, once free MSI78 derivatives lose antimicrobial activity in this medium [76]. Also, studying the time-dependent activity of AMP-NP using a time-kill assay would be valuable to see if the antimicrobial activity of the grafted AMP changes over longer periods. Also, it would be important to test how is the release profile of AMP-NPs from MC hydrogels.

In an overall perspective of this work, we can conclude that MC hydrogels show promising results as smart delivery systems, for the release bactericidal compounds (AMP-NP) in response to an endogenous stimulus (ROS), to fight bacterial infections in chronic wounds.

7. References

[1] R. Zhao, H. Liang, E. Clarke, C. Jackson, and M. Xue, “Inflammation in Chronic Wounds,” *Int J Mol Sci*, vol. 17, no. 12, p. 2085, Dec. 2016, doi: 10.3390/ijms17122085.

[2] P. M. Alves, C. C. Barrias, P. Gomes, and M. C. L. Martins, “Smart biomaterial-based systems for intrinsic stimuli-responsive chronic wound management,” *Mater Today Chem*, vol. 22, p. 100623, Dec. 2021, doi: 10.1016/j.mtchem.2021.100623.

[3] N. J. Percival, “Classification of Wounds and their Management,” *Surgery (Oxford)*, vol. 20, no. 5, pp. 114–117, May 2002, doi: 10.1383/surg.20.5.114.14626.

[4] J. M. Reinke and H. Sorg, “Wound Repair and Regeneration,” *European Surgical Research*, vol. 49, no. 1, pp. 35–43, 2012, doi: 10.1159/000339613.

[5] M. Xue, R. Zhao, H. Lin, and C. Jackson, “Delivery systems of current biologicals for the treatment of chronic cutaneous wounds and severe burns,” *Adv Drug Deliv Rev*, vol. 129, pp. 219–241, Apr. 2018, doi: 10.1016/j.addr.2018.03.002.

[6] K. Las Heras, M. Igartua, E. Santos-Vizcaino, and R. M. Hernandez, “Chronic wounds: Current status, available strategies and emerging therapeutic solutions,” *Journal of Controlled Release*, vol. 328, pp. 532–550, Dec. 2020, doi: 10.1016/j.jconrel.2020.09.039.

[7] I. Firlar, M. Altunbek, C. McCarthy, M. Ramalingam, and G. Camci-Unal, “Functional Hydrogels for Treatment of Chronic Wounds,” *Gels*, vol. 8, no. 2, p. 127, Feb. 2022, doi: 10.3390/gels8020127.

[8] P. Martin and R. Nunan, “Cellular and molecular mechanisms of repair in acute and chronic wound healing,” *British Journal of Dermatology*, vol. 173, no. 2, pp. 370–378, Aug. 2015, doi: 10.1111/bjd.13954.

[9] A. Stojadinovic, J. W. Carlson, G. S. Schultz, T. A. Davis, and E. A. Elster, “Topical advances in wound care,” *Gynecol Oncol*, vol. 111, no. 2, pp. S70–S80, Nov. 2008, doi: 10.1016/j.ygyno.2008.07.042.

[10] H. S. Kim, X. Sun, J.-H. Lee, H.-W. Kim, X. Fu, and K. W. Leong, “Advanced drug delivery systems and artificial skin grafts for skin wound healing,” *Adv Drug Deliv Rev*, vol. 146, pp. 209–239, Jun. 2019, doi: 10.1016/j.addr.2018.12.014.

[11] O. Soehnlein, S. Steffens, A. Hidalgo, and C. Weber, “Neutrophils as protagonists and targets in chronic inflammation,” *Nat Rev Immunol*, vol. 17, no. 4, pp. 248–261, Apr. 2017, doi: 10.1038/nri.2017.10.

[12] E. Kolaczkowska and P. Kubes, “Neutrophil recruitment and function in health and inflammation,” *Nat Rev Immunol*, vol. 13, no. 3, pp. 159–175, Mar. 2013, doi: 10.1038/nri3399.

[13] Y. Guo *et al.*, “AGEs Induced Autophagy Impairs Cutaneous Wound Healing via Stimulating Macrophage Polarization to M1 in Diabetes,” *Sci Rep*, vol. 6, no. 1, p. 36416, Nov. 2016, doi: 10.1038/srep36416.

[14] I. Mothe-Satney *et al.*, “Adipocytes Secrete Leukotrienes,” *Diabetes*, vol. 61, no. 9, pp. 2311–2319, Sep. 2012, doi: 10.2337/db11-1455.

[15] J. Cha *et al.*, “Fibroblasts from non-healing human chronic wounds show decreased expression of βig-h3, a TGF-β inducible protein,” *J Dermatol Sci*, vol. 50, no. 1, pp. 15–23, Apr. 2008, doi: 10.1016/j.jdermsci.2007.10.010.

[16] A. Friedman and N. Siewe, “Mathematical Model of Chronic Dermal Wounds in Diabetes and Obesity,” *Bull Math Biol*, vol. 82, no. 10, p. 137, Oct. 2020, doi: 10.1007/s11538-020-00815-x.

[17] M. Fierheller and R. G. Sibbald, “A Clinical Investigation into the Relationship between Increased Periwound Skin Temperature and Local Wound Infection in Patients with Chronic Leg Ulcers,” *Adv Skin Wound Care*, vol. 23, no. 8, pp. 369–379, Aug. 2010, doi: 10.1097/01.ASW.0000383197.28192.98.

[18] C. Dunnill *et al.*, “Reactive oxygen species (ROS) and wound healing: the functional role of ROS and emerging ROS-modulating technologies for

augmentation of the healing process," *Int Wound J*, vol. 14, no. 1, pp. 89–96, Feb. 2017, doi: 10.1111/iwj.12557.

[19] T. N. Demidova-Rice, M. R. Hamblin, and I. M. Herman, "Acute and Impaired Wound Healing," *Adv Skin Wound Care*, vol. 25, no. 7, pp. 304–314, Jul. 2012, doi: 10.1097/01.ASW.0000416006.55218.d0.

[20] L. J. Bessa, P. Fazii, M. Di Giulio, and L. Cellini, "Bacterial isolates from infected wounds and their antibiotic susceptibility pattern: some remarks about wound infection," *Int Wound J*, vol. 12, no. 1, pp. 47–52, Feb. 2015, doi: 10.1111/iwj.12049.

[21] K. Kirketerp-Møller *et al.*, "Distribution, Organization, and Ecology of Bacteria in Chronic Wounds," *J Clin Microbiol*, vol. 46, no. 8, pp. 2717–2722, Aug. 2008, doi: 10.1128/JCM.00501-08.

[22] W. M. Dunne, "Bacterial Adhesion: Seen Any Good Biofilms Lately?," *Clin Microbiol Rev*, vol. 15, no. 2, pp. 155–166, Apr. 2002, doi: 10.1128/CMR.15.2.155-166.2002.

[23] H.-C. Flemming and J. Wingender, "The biofilm matrix," *Nat Rev Microbiol*, vol. 8, no. 9, pp. 623–633, Sep. 2010, doi: 10.1038/nrmicro2415.

[24] Y.-K. Wu, N.-C. Cheng, and C.-M. Cheng, "Biofilms in Chronic Wounds: Pathogenesis and Diagnosis," *Trends Biotechnol*, vol. 37, no. 5, pp. 505–517, May 2019, doi: 10.1016/j.tibtech.2018.10.011.

[25] M. Richard J.Friedman, *Handbook of Bacterial Adhesion- Pricinples, Methods, and Applications*. Springer Science+ Business Media, LLC, 2000. Accessed: Jun. 23, 2025. [Online]. Available: https://books.google.pt/books?hl=pt-PT&lr=&id=YXz5BwAAQBAJ&oi=fnd&pg=PR7&dq=Handbook+of+Bacterial+Adhesion:+Principles,+Methods,+and+Applications&ots=2_2UUc1xDF&sig=mcu4C8INHDRiAUR4SqBuGuNEZP0&redir_esc=y#v=onepage&q=Handbook%20of%20Bacterial%20Adhesion%3A%20Principles%2C%20Methods%2C%20and%20Applications&f=false

[26] S. Wagner *et al.*, "Novel Strategies for the Treatment of *Pseudomonas aeruginosa* Infections," *J Med Chem*, vol. 59, no. 13, pp. 5929–5969, Jul. 2016, doi: 10.1021/acs.jmedchem.5b01698.

[27] G. O'Toole, H. B. Kaplan, and R. Kolter, "Biofilm Formation as Microbial Development," *Annu Rev Microbiol*, vol. 54, no. 1, pp. 49–79, Oct. 2000, doi: 10.1146/annurev.micro.54.1.49.

[28] J. Wang *et al.*, "NIR-II emissive biohybrid nanovesicles as mild-temperature photothermal antibiofilm agents against acute bacterial skin and skin-structure infections," *Interdisciplinary Medicine*, vol. 3, no. 1, Jan. 2025, doi: 10.1002/INMD.20240053.

[29] T. Strateva and D. Yordanov, "Pseudomonas aeruginosa – a phenomenon of bacterial resistance," *J Med Microbiol*, vol. 58, no. 9, pp. 1133–1148, Sep. 2009, doi: 10.1099/jmm.0.009142-0.

[30] I. Omwenga *et al.*, "Antimicrobial Usage and Detection of Multidrug-Resistant *Staphylococcus aureus* , Including Methicillin-Resistant Strains in Raw Milk of Livestock from Northern Kenya," *Microbial Drug Resistance*, vol. 27, no. 6, pp. 843–854, Jun. 2021, doi: 10.1089/mdr.2020.0252.

[31] K. E. Grooters *et al.*, "Strategies for combating antibiotic resistance in bacterial biofilms," *Front Cell Infect Microbiol*, vol. 14, Jan. 2024, doi: 10.3389/fcimb.2024.1352273.

[32] R. Gobi, P. Ravichandiran, R. S. Babu, and D. J. Yoo, "Biopolymer and Synthetic Polymer-Based Nanocomposites in Wound Dressing Applications: A Review," *Polymers (Basel)*, vol. 13, no. 12, p. 1962, Jun. 2021, doi: 10.3390/polym13121962.

[33] E. Rezvani Ghomi, S. Khalili, S. Nouri Khorasani, R. Esmaeely Neisiany, and S. Ramakrishna, "Wound dressings: Current advances and future directions," *J Appl Polym Sci*, vol. 136, no. 27, Jul. 2019, doi: 10.1002/app.47738.

[34] I. Negut, V. Grumezescu, and A. M. Grumezescu, "Treatment Strategies for Infected Wounds," *Molecules*, vol. 23, no. 9, p. 2392, Sep. 2018, doi: 10.3390/molecules23092392.

[35] H. P. Felgueiras and M. T. P. Amorim, "Functionalization of electrospun polymeric wound dressings with antimicrobial peptides," *Colloids Surf B Biointerfaces*, vol. 156, pp. 133–148, Aug. 2017, doi: 10.1016/j.colsurfb.2017.05.001.

[36] V. Jones, J. E. Grey, and K. G. Harding, “Wound dressings,” *BMJ*, vol. 332, no. 7544, pp. 777–780, Apr. 2006, doi: 10.1136/bmj.332.7544.777.

[37] M. T. Khorasani, A. Joorabloo, A. Moghaddam, H. Shamsi, and Z. MansooriMoghadam, “Incorporation of ZnO nanoparticles into heparinised polyvinyl alcohol/chitosan hydrogels for wound dressing application,” *Int J Biol Macromol*, vol. 114, pp. 1203–1215, Jul. 2018, doi: 10.1016/j.ijbiomac.2018.04.010.

[38] R. Rakhshaei and H. Namazi, “A potential bioactive wound dressing based on carboxymethyl cellulose/ZnO impregnated MCM-41 nanocomposite hydrogel,” *Materials Science and Engineering: C*, vol. 73, pp. 456–464, Apr. 2017, doi: 10.1016/j.msec.2016.12.097.

[39] J.-M. Wu, Y. Liu, H.-Y. Han, and Z.-Y. Song, “Recent advances in endogenous and exogenous stimuli-responsive nanoplatforms for bacterial infection treatment,” *Biomedical Engineering Communications*, vol. 2, no. 1, p. 2, 2023, doi: 10.53388/BMEC2023002.

[40] P. Nasatto, F. Pignon, J. Silveira, M. Duarte, M. Noseda, and M. Rinaudo, “Methylcellulose, a Cellulose Derivative with Original Physical Properties and Extended Applications,” *Polymers (Basel)*, vol. 7, no. 5, pp. 777–803, Apr. 2015, doi: 10.3390/polym7050777.

[41] H. Q. LIU, L. N. ZHANG, A. TAKARAGI, and T. MIYAMOTO, “Effect of substituent distribution on water solubility of O-methylcellulose,” *Cellulose*, vol. 4, no. 4, pp. 321–327, 1997, doi: 10.1023/A:1018404426960.

[42] A. Forghani and R. Devireddy, “Methylcellulose Based Thermally Reversible Hydrogels,” 2018, pp. 41–51. doi: 10.1007/978-1-4939-7799-4_5.

[43] Q. Zhang, C. Weber, U. S. Schubert, and R. Hoogenboom, “Thermoresponsive polymers with lower critical solution temperature: from fundamental aspects and measuring techniques to recommended turbidimetry conditions,” *Mater Horiz*, vol. 4, no. 2, pp. 109–116, 2017, doi: 10.1039/C7MH00016B.

[44] “Basics of rheology.” Accessed: Apr. 22, 2025. [Online]. Available: https://wiki.anton-paar.com/en/basics-of-rheology/#references-and-further-reading

[45] H. Ramli, N. F. A. Zainal, M. Hess, and C. H. Chan, “Basic principle and good practices of rheology for polymers for teachers and beginners,” *Chemistry Teacher International*, vol. 4, no. 4, pp. 307–326, Dec. 2022, doi: 10.1515/cti-2022-0010.

[46] Kevin Whitcomb, “Determining the Linear Viscoelastic Region in Oscillatory Measurements.” Accessed: Apr. 22, 2025. [Online]. Available: https://www.tainstruments.com/pdf/literature/RH107.pdf

[47] P. Zheng, L. Li, X. Hu, and X. Zhao, “Sol–gel transition of methylcellulose in phosphate buffer saline solutions,” *J Polym Sci B Polym Phys*, vol. 42, no. 10, pp. 1849–1860, May 2004, doi: 10.1002/polb.20070.

[48] M. Jergitsch, Z. Alluè-Mengual, R. A. Perez, and M. A. Mateos-Timoneda, “A systematic approach to improve printability and cell viability of methylcellulose-based bioinks,” *Int J Biol Macromol*, vol. 253, p. 127461, Dec. 2023, doi: 10.1016/j.ijbiomac.2023.127461.

[49] T. J. James, M. A. Hughes, G. W. Cherry, and R. P. Taylor, “Evidence of oxidative stress in chronic venous ulcers,” *Wound Repair and Regeneration*, vol. 11, no. 3, pp. 172–176, May 2003, doi: 10.1046/j.1524-475X.2003.11304.x.

[50] Q. Qu *et al.*, “Triggered Release from Cellulose Microparticles Inspired by Wood Degradation by Fungi,” *ACS Sustain Chem Eng*, vol. 9, no. 1, pp. 387–397, Jan. 2021, doi: 10.1021/acssuschemeng.0c07514.

[51] C. de Gracia Lux *et al.*, “Biocompatible Polymeric Nanoparticles Degrade and Release Cargo in Response to Biologically Relevant Levels of Hydrogen Peroxide,” *J Am Chem Soc*, vol. 134, no. 38, pp. 15758–15764, Sep. 2012, doi: 10.1021/ja303372u.

[52] K. E. Broaders, S. Grandhe, and J. M. J. Fréchet, “A Biocompatible Oxidation-Triggered Carrier Polymer with Potential in Therapeutics,” *J Am Chem Soc*, vol. 133, no. 4, pp. 756–758, Feb. 2011, doi: 10.1021/ja110468v.

[53] M. K. Gupta, T. A. Meyer, C. E. Nelson, and C. L. Duvall, “Poly(PS-b-DMA) micelles for reactive oxygen species triggered drug release,” *Journal of Controlled Release*, vol. 162, no. 3, pp. 591–598, Sep. 2012, doi: 10.1016/j.jconrel.2012.07.042.

[54] J. Duan and D. L. Kasper, “Oxidative depolymerization of polysaccharides by reactive oxygen/nitrogen species,” *Glycobiology*, vol. 21, no. 4, pp. 401–409, Apr. 2011, doi: 10.1093/glycob/cwq171.

[55] Q. Qu *et al.*, “Triggered Release from Cellulose Microparticles Inspired by Wood Degradation by Fungi,” *ACS Sustain Chem Eng*, vol. 9, no. 1, pp. 387–397, Jan. 2021, doi: 10.1021/acssuschemeng.0c07514.

[56] S. Story *et al.*, “Understanding Antisense Oligonucleotide Efficiency in Inhibiting Prokaryotic Gene Expression,” *ACS Infect Dis*, vol. 10, no. 3, pp. 971–987, Mar. 2024, doi: 10.1021/acsinfecdis.3c00645.

[57] P. M. D. Moreno and A. P. PÃªgo, “Therapeutic antisense oligonucleotides against cancer: hurdling to the clinic,” *Front Chem*, vol. 2, Oct. 2014, doi: 10.3389/fchem.2014.00087.

[58] M. L. Stephenson and P. C. Zamecnik, “Inhibition of Rous sarcoma viral RNA translation by a specific oligodeoxyribonucleotide.,” *Proceedings of the National Academy of Sciences*, vol. 75, no. 1, pp. 285–288, Jan. 1978, doi: 10.1073/pnas.75.1.285.

[59] D. A. Giljohann, D. S. Seferos, P. C. Patel, J. E. Millstone, N. L. Rosi, and C. A. Mirkin, “Oligonucleotide Loading Determines Cellular Uptake of DNA-Modified Gold Nanoparticles,” *Nano Lett*, vol. 7, no. 12, pp. 3818–3821, Dec. 2007, doi: 10.1021/nl072471q.

[60] P. C. Patel, D. A. Giljohann, D. S. Seferos, and C. A. Mirkin, “Peptide antisense nanoparticles,” *Proceedings of the National Academy of Sciences*, vol. 105, no. 45, pp. 17222–17226, Nov. 2008, doi: 10.1073/pnas.0801609105.

[61] A. Astriab-Fisher, D. S. Sergueev, M. Fisher, B. Ramsay Shaw, and R. L. Juliano, “Antisense inhibition of P-glycoprotein expression using peptide–oligonucleotide conjugates,” *Biochem Pharmacol*, vol. 60, no. 1, pp. 83–90, Jul. 2000, doi: 10.1016/S0006-2952(00)00310-5.

[62] A. R. P. Silva *et al.*, “Recent advances in the design of antimicrobial peptide conjugates,” *J Mater Chem B*, vol. 10, no. 19, pp. 3587–3600, 2022, doi: 10.1039/D1TB02757C.

[63] A. Rai *et al.*, “Antimicrobial peptide-based materials: opportunities and challenges,” *J Mater Chem B*, vol. 10, no. 14, pp. 2384–2429, 2022, doi: 10.1039/D1TB02617H.

[64] C. Monteiro *et al.*, “AMP–Chitosan Coating with Bactericidal Activity in the Presence of Human Plasma Proteins,” *Molecules*, vol. 25, no. 13, p. 3046, Jul. 2020, doi: 10.3390/molecules25133046.

[65] M. N. Melo, R. Ferre, and M. A. R. B. Castanho, “Antimicrobial peptides: linking partition, activity and high membrane-bound concentrations,” *Nat Rev Microbiol*, vol. 7, no. 3, pp. 245–250, Mar. 2009, doi: 10.1038/nrmicro2095.

[66] B. Xiao *et al.*, “Unlocking the Potential of Antimicrobial Peptides: Cutting-Edge Advances and Therapeutic Potential in Combating Bacterial Keratitis,” *Bioconjug Chem*, vol. 36, no. 3, pp. 311–331, Mar. 2025, doi: 10.1021/acs.bioconjchem.4c00594.

[67] P. M. Alves, C. C. Barrias, P. Gomes, and M. C. L. Martins, “How can biomaterial-conjugated antimicrobial peptides fight bacteria and be protected from degradation?,” *Acta Biomater*, vol. 181, pp. 98–116, Jun. 2024, doi: 10.1016/j.actbio.2024.04.043.

[68] L. M. Gottler and A. Ramamoorthy, “Structure, membrane orientation, mechanism, and function of pexiganan — A highly potent antimicrobial peptide designed from magainin,” *Biochimica et Biophysica Acta (BBA) - Biomembranes*, vol. 1788, no. 8, pp. 1680–1686, Aug. 2009, doi: 10.1016/j.bbamem.2008.10.009.

[69] H. Cohen *et al.*, “Interaction of Pexiganan (MSI-78)-Derived Analogues Reduces Inflammation and TLR4-Mediated Cytokine Secretion: A Comparative Study,” *ACS Omega*, vol. 8, no. 20, pp. 17856–17868, May 2023, doi: 10.1021/acsomega.3c00850.

[70] R. Singh and J. W. Lillard, “Nanoparticle-based targeted drug delivery,” *Exp Mol Pathol*, vol. 86, no. 3, pp. 215–223, Jun. 2009, doi: 10.1016/j.yexmp.2008.12.004.

[71] G. Adamo, S. Campora, and G. Ghersi, “Functionalization of nanoparticles in specific targeting and mechanism release,” in *Nanostructures for Novel*

Therapy, Elsevier, 2017, pp. 57–80. doi: 10.1016/B978-0-323-46142-9.00003-7.

[72] X. Zhu, A. F. Radovic-Moreno, J. Wu, R. Langer, and J. Shi, “Nanomedicine in the management of microbial infection – Overview and perspectives,” *Nano Today*, vol. 9, no. 4, pp. 478–498, Aug. 2014, doi: 10.1016/j.nantod.2014.06.003.

[73] D. P. K. Lankveld *et al.*, “The kinetics of the tissue distribution of silver nanoparticles of different sizes,” *Biomaterials*, vol. 31, no. 32, pp. 8350–8361, Nov. 2010, doi: 10.1016/j.biomaterials.2010.07.045.

[74] H. L. Karlsson, P. Cronholm, J. Gustafsson, and L. Möller, “Copper Oxide Nanoparticles Are Highly Toxic: A Comparison between Metal Oxide Nanoparticles and Carbon Nanotubes,” *Chem Res Toxicol*, vol. 21, no. 9, pp. 1726–1732, Sep. 2008, doi: 10.1021/tx800064j.

[75] A. M. Schrand, M. F. Rahman, S. M. Hussain, J. J. Schlager, D. A. Smith, and A. F. Syed, “Metal-based nanoparticles and their toxicity assessment,” *WIREs Nanomedicine and Nanobiotechnology*, vol. 2, no. 5, pp. 544–568, Sep. 2010, doi: 10.1002/wnan.103.

[76] A. M. Ramôa *et al.*, “Antimicrobial peptide-grafted PLGA-PEG nanoparticles to fight bacterial wound infections,” *Biomater Sci*, vol. 11, no. 2, pp. 499–508, 2023, doi: 10.1039/D2BM01127A.

[77] F. Motsoene, H. Abrahamse, and S. S. Dhilip Kumar, “Multifunctional lipid-based nanoparticles for wound healing and antibacterial applications: A review,” *Adv Colloid Interface Sci*, vol. 321, p. 103002, Nov. 2023, doi: 10.1016/j.cis.2023.103002.

[78] Z. Si *et al.*, “Antimicrobial Effect of a Novel Chitosan Derivative and Its Synergistic Effect with Antibiotics,” *ACS Appl Mater Interfaces*, vol. 13, no. 2, pp. 3237–3245, Jan. 2021, doi: 10.1021/acsami.0c20881.

[79] P. Li *et al.*, “Cationic Peptidopolysaccharides Show Excellent Broad-Spectrum Antimicrobial Activities and High Selectivity,” *Advanced Materials*, vol. 24, no. 30, pp. 4130–4137, Aug. 2012, doi: 10.1002/adma.201104186.

[80] J. C. Lee *et al.*, “Exploring Maleimide-Based Nanoparticle Surface Engineering to Control Cellular Interactions,” *ACS Appl Nano Mater*, vol. 3, no. 3, pp. 2421–2429, Mar. 2020, doi: 10.1021/acsanm.9b02541.

[81] António Ramôa, “Antimicrobial Nanoparticles to Fight Bacterial Wound Infections,” 2021.

[82] A. Albisa, E. Piacentini, V. Sebastian, M. Arruebo, J. Santamaria, and L. Giorno, “Preparation of Drug-Loaded PLGA-PEG Nanoparticles by Membrane-Assisted Nanoprecipitation,” *Pharm Res*, vol. 34, no. 6, pp. 1296–1308, Jun. 2017, doi: 10.1007/s11095-017-2146-y.

[83] I. Wiegand, K. Hilpert, and R. E. W. Hancock, “Agar and broth dilution methods to determine the minimal inhibitory concentration (MIC) of antimicrobial substances,” *Nat Protoc*, vol. 3, no. 2, pp. 163–175, Feb. 2008, doi: 10.1038/nprot.2007.521.

[84] PEDRO MIGUEL PINTO BASTO ALVES, “BIOHEAL – BIOACTIVATABLE MODULAR DRESSING FOR CHRONIC INFECTED WOUNDS,” FEUP, Porto, 2024.

[85] C. Monteiro *et al.*, “A 17-mer Membrane-Active MSI-78 Derivative with Improved Selectivity toward Bacterial Cells,” *Mol Pharm*, vol. 12, no. 8, pp. 2904–2911, Aug. 2015, doi: 10.1021/acs.molpharmaceut.5b00113.

[86] G. Wei, H. Xu, P. T. Ding, S. M. Li, and J. M. Zheng, “Thermosetting gels with modulated gelation temperature for ophthalmic use: the rheological and gamma scintigraphic studies,” *Journal of Controlled Release*, vol. 83, no. 1, pp. 65–74, Sep. 2002, doi: 10.1016/S0168-3659(02)00175-X.

[87] Q. Sun *et al.*, “Recent advances on endogenous/exogenous stimuli-triggered nanoplatforms for enhanced chemodynamic therapy,” *Coord Chem Rev*, vol. 451, p. 214267, Jan. 2022, doi: 10.1016/j.ccr.2021.214267.

[88] P. Guo *et al.*, “Facile Fabrication of Methylcellulose/PLA Membrane with Improved Properties,” *Coatings*, vol. 10, no. 5, p. 499, May 2020, doi: 10.3390/coatings10050499.

[89] “Product Name: Methoxy Poly(ethylene glycol)-b-Poly(lactide-co-glycolide) (~3,000:36,000 Da) (Lot#: 60523EJF-A).” Accessed: Jun. 13, 2025. [Online]. Available: https://akinainc.com/polyscitech/COA/AK029-60523EJF-A.pdf